CHARACTERIZATION OF THE INTERDIFFUSION MICROSTRUCTURE, A15 LAYER GROWTH AND STOICHIOMETRY IN TUBE-TYPE Nb_3Sn COMPOSITES

A Thesis

Presented in Partial Fulfillment of the Requirements for

The Degree of Master of Science in the Graduate

School of the Ohio State University

By

Vishal Ryan Nazareth, B. E.

*****

The Ohio State University
2008

Approved by

Adviser
Graduate Program in Materials Science and Engineering

Masters Examination Committee

Professor Mike Sumption, Adviser

Professor John Morral, Adviser

Professor Katharine Flores

Adviser
Graduate Program in Materials Science and Engineering

ABSTRACT

Multifilamentary tube-type Nb_3Sn composites were characterized in terms of their interdiffusion microstructure, A15 layer growth and stoichiometry in an attempt to enhance their properties. These composites were fabricated using Nb-7.5wt% Ta alloy tubes with varying subelement Sn/Cu ratios and had filament counts ranging from 61-167. Samples were heat treated between 650-800°C for varying intervals of time up to 250 hours. Phase evolution leading to A15 formation as well as the growth kinetics of the fine grain A15 was analyzed as a function of reaction time to investigate the effects of temperature as well as the initial subelement Sn/Cu ratio. The layer growth exponent *n*, growth constant *k* and growth rates at different heat treatment times were also determined at 650°C and 725°C. An analytical model, to aid in predicting the ratio of fine to coarse grain A15 for various initial subelement Sn/Cu ratios was discussed. The predictions were compared with the experimentally obtained data.

Compositional analysis was performed on these strands using the SEM-EDS technique to correlate the effect of heat treatment temperature on the Sn compositions across the fine and coarse grain A15. The effect of the initial subelement Sn/Cu ratios on the Sn compositions was studied for a given heat treatment temperature. The Cu levels across the A15 phase as a function of reaction temperature was also determined. A

detailed analysis of the grain morphology and grain size of the fine and coarse grain A15 was performed at various reaction temperatures with the aid of fracture SEM samples. The activation energy for grain growth was also calculated from the experimental data. In addition the non-Cu critical current densities (J_c) and the upper critical field (B_{c2}) were measured for these composites.

ACKNOWLEDGMENTS

It gives me great pleasure to thank many people who have made my time at the Ohio State University a productive and memorable one. Foremost, I would like to express my sincere gratitude to my advisor, Dr. Michael Sumption for giving me an opportunity to work with him and the entire group at LASM (Laboratory for Applied Superconductivity and Magnetism). His cheerful personality, constant encouragement, guidance and support have been a great asset all through my research work.

I am also deeply indebted to my advisor, Dr. John Morral for his detailed discussions and constructive comments which have been of great value to me. His wide knowledge of the subject and ability to explain things clearly and concisely made the subject intriguing and easier to grasp.

I also wish to express my sincere thanks to Dr. Edward W. Collings for his invaluable comments and insights throughout this work.

Many thanks to Michael Tomsic (Hyperterch Research Inc.), Eric Gregory (Supergenics LLC) and the entire team for providing the superconducting samples that served as the basis for this study. I am also very appreciative of Xuan Peng (Hypertech Research Inc.) for sample fabrication, heat treatments and assistance with electron microscopy.

I would like to thank the technical staff in the Materials Science and Engineering department at the Ohio State University especially Steve Bright, Cameron Begg and Gary Dodge for their assistance in sample preparation, optical and electron microscopy.

I thank all my friends and fellow graduate students Mohit Bhatia, Scot Bohnenstiehl, Rakesh Dhaka and Michael Susner for making my time at LASM an enjoyable one.

Lastly, and most importantly, I would like to thank my parents, brother and family members for their motivation, love and constant support throughout my endeavors without which I would not be where I am.

VITA

August 17, 1983. . . . . Born – Mumbai, India

2001-2005. . . . . B.E, Metallurgy and Materials Engineering,
National Institute of Technology, Karnataka, India

2005-2006. . . . . Materials Engineer, Engineering Research Center,
Tata Motors, Pune, India

2007-2008. . . . . Graduate Research Associate,
The Ohio State University, USA

FIELDS OF STUDY

Major Field: Materials Science and Engineering

TABLE OF CONTENTS

LIST OF TABLES

LIST OF FIGURES

Figure Page

CHAPTER 1

INTRODUCTION TO SUPERCONDUCTIVITY

1.1 Introduction

Intermetallic Nb_3Sn having an A15 crystal structure is currently the preferred low temperature superconductor for the generation of high magnetic fields [1-3]. The ability of this material to carry high currents in strong magnetic fields makes it the material of choice for winding coils intended for high field applications, for example, particle accelerators, fusion reactors and nuclear magnetic resonance magnets. Extensive research has been carried out especially in the past decade in order to improve the superconducting properties and enhance the performance boundaries of theses composites. Presently the non-Cu critical current density achieved in state of the art Nb_3Sn composites at 4.2 K, 12 T is around 3000 A/mm^2 [4].

Nb_3Sn traces its history back to the year 1954 when it was discovered by Matthias [5] subsequent to the discovery of V_3Si. Even though this material was found to carry large current densities at high fields it has seen limited applications. This has been mainly due to the brittle nature of the A15 coupled with the high cost of manufacturing and the strain sensitivity of the A15 phase [6]. Over the previous decades, the preferred choice of

material for high field applications has been NbTi, primarily due to its high ductility and ease of manufacture. However, NbTi has been optimized, and is operating near the intrinsic limits of its superconducting properties. As machine demands continue to increase, the focus of attention has shifted over the past decade towards the development of Nb_3Sn composites which have higher performance limits. Importantly for high field applications, the upper critical field (B_{c2}) has reached values nearing 30 T at 4.2 K which is almost twice that available with NbTi composites.

Nb_3Sn composites can be manufactured by a wide variety of different processes, such as the bronze route, the internal-Sn route, the powder in tube (PIT) route, and tube-type designs (this route has also been called the solid-liquid diffusion process). These processes differ in terms of their initial starting materials, internal strand geometry, and even the A15 formation path, these differences will be discussed in detail in Chapter 2. However they follow a similar two step approach in forming the brittle Nb_3Sn phase. In step one theses composites are fabricated by a number of different processes such as wire drawing and extrusion (used only for bronze and internal-Sn composites). Subsequent to this the composites are heat treated at elevated temperatures ranging from about 650-725°C to form the A15 phase by the process of reactive diffusion of the Sn atoms with the Nb matrix.

The main efforts of the Nb_3Sn conductor development are directed towards producing cost effective magnets with high performance [7]. In order to achieve high critical current densities (J_c) and upper critical fields (B_{c2}) a detailed understanding of the phase evolution during heat treatment as well as the effects of the final microstructure on the superconducting properties is helpful. This would enable one to tailor the

microstructure to obtain the desired properties. The main challenge in producing superior quality A15 by the above manufacturing methods is in obtaining stoichiometric A15 having a fine grain size. A15 with Sn contents close to the stoichiometric value have been found to have a superior B_{c2} [8] where as the fine grain structure provides for strong flux pinning and in turn an improved J_c. However the use of aggressive heat treatments (involving high temperatures and longer reaction times) to obtain stoichiometric A15 would invariably result in significant grain growth due to enhanced kinetics. Thus optimization of the heat treatment process to achieve a fine balance in these properties is of utmost importance. As seen in the literature a number of ternary additions especially transition elements such as Ti and Ta have also improved the superconducting properties [9-13].

In the present work multifilamentary tube-type composites with ternary additions mainly in the form of Ta were fabricated and characterized in terms of their microstructure. A complete review of the microstructure-property characterization in these composites alone appears to be lacking in the literature. In Chapter 4, phase evolution in these composites is presented as a function of reaction time to investigate the effects of temperature as well as the initial subelement Sn/Cu ratio on phase formation. Layer growth was also determined at different temperatures and is compared with PIT and internal-Sn strands. The layer growth exponent n as well as the growth constant k is also evaluated and growth rates at different heat treatment times are also presented. An analytical model that could be used in predicting the ratio of fine to coarse grain A15 for various initial subelement Sn/Cu ratios is discussed and the results are compared with the experimentally obtained data.

In Chapter 5 a detailed investigation of composition profiles across the A15 phase as a function of the heat treatment temperature with the aid of a Scanning Electron Microscope fitted with an Energy Dispersive X-Ray Spectroscopy detector is described. The effects of the initial subelement Sn/Cu ratio on the A15 composition as well as the Cu levels in the A15 as a function of temperature are described. Grain morphology as well as grain growth as a function of heat treatment temperature are reported along with activation energy for growth.

1.2 Overview of Superconductivity

Superconductivity in its simplest form can be defined as the zero electrical resistance state of a material and was discovered in the year 1911 by Kamerlingh Onnes after he had achieved the liquefaction of helium [14]. He showed that the DC electrical resistivity disappeared all together when mercury was cooled below a critical temperature T_c of about 4.2 K (Figure 1.1). The decay time of electrical current in a superconducting ring over long periods of time has yielded time constants of over 10^5 years [15]. Superconductivity is known to occur in a wide range of metals and alloys, excluding noble and ferromagnetic materials. Figure 1.2 shows the temperature dependence of heat capacity of materials near the superconducting transition temperature. When a material is cooled at low temperatures there is a gradual decrease in the heat capacity, however a sudden increase in heat capacity of the order of 2-3 times is observed when a superconducting material is cooled below T_c.

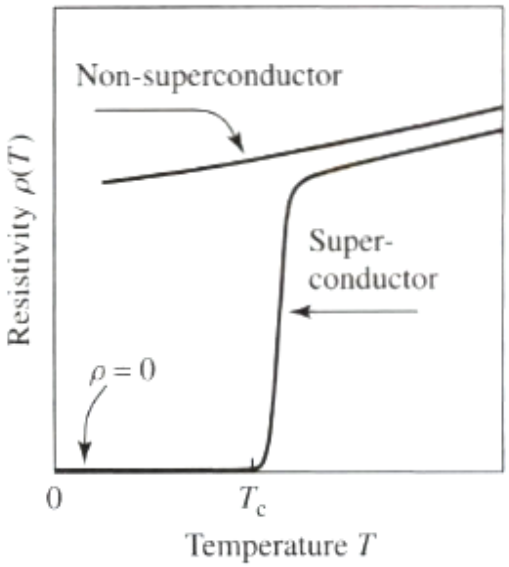

Figure 1.1 Illustration of the variation in the resistivity for a superconducting and non superconducting material, a sudden drop was observed at the transition temperature for a superconductor [15].

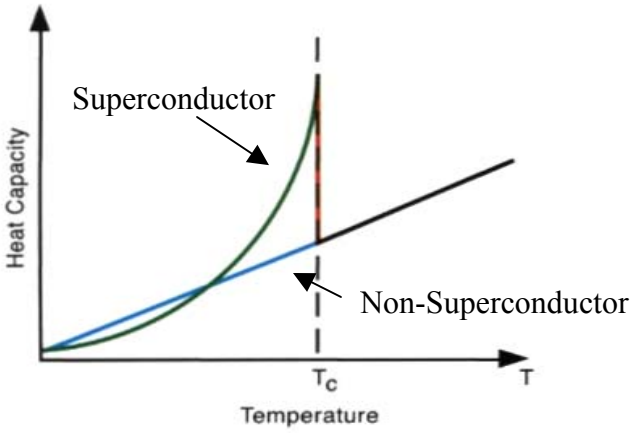

Figure 1.2 Variation in heat capacity for a superconducting as well as a non superconducting material. A sudden jump in the heat capacity at the transition temperature was observed in the case of a superconductor [16].

The superconducting state of a material can be defined by three main parameters namely the critical temperature (T_c), the critical magnetic field (B_{c2}) and the critical current (J_c). Figure 1.3 shows the three dimensional plot which defines the boundaries of a superconductor. For any given set of conditions lying within the boundary the material is completely superconducting, however if the temperature, current or magnetic field were increased beyond a certain value to a region outside the boundary a transition from the superconducting to normal state was observed. Equation (1.10) gives the variation of critical field (H_c) as a function of temperature (T) and is most accurate only when T is close to T_c. Here (H_0) is the field at 0 K.

$$H_c \approx H_0[1-\frac{T}{T_C}]^2 \tag{1.10}$$

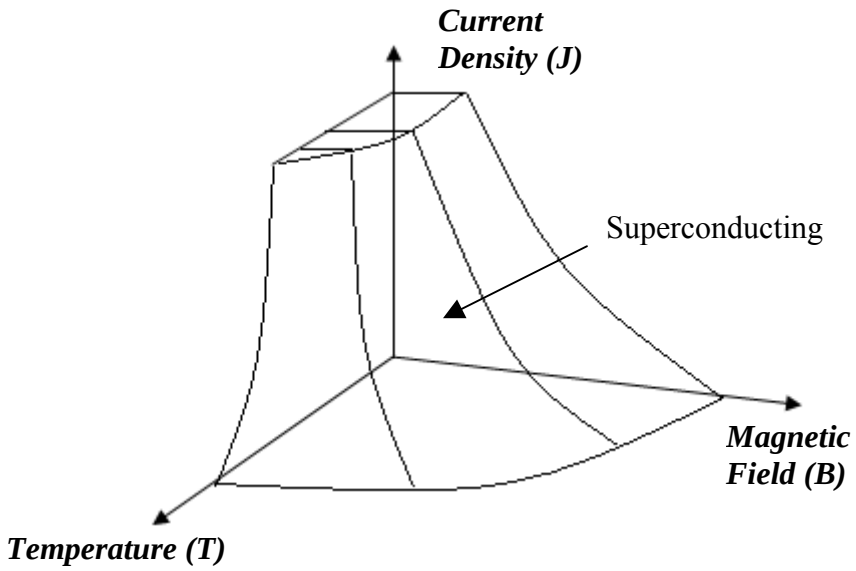

Figure 1.3 The three dimensional space for a superconductor.

Another important characteristic feature of a superconductor which makes it uniquely different from that of a normal conductor was the abrupt change in the magnetic susceptibility from a small positive paramagnetic value to that of perfect diamagnetism below the critical temperature *(T_c)*. This phenomenon was discovered in the year 1933 by Meissner and Ochsenfeld and is known as the Meissner effect [17].

In the Meissner state a sudden expulsion of the magnetic field from within the superconductor is observed when the sample is cooled below the critical temperature [18]. The magnetic field is excluded from the superconductor independent of whether the applied field is present in the material before cooling below the critical temperature. The constitutive equation for a magnetic body in the superconducting state can be given by equation (1.11). Here B (T) is the magnetic field induction within the sample, H (A/m) is the applied magnetic field, M (A/m) is the magnetization due to applied magnetic field and μ_o was permeability of free space. For a Type-I superconductors, $B = 0$, implies $M = -H$ in the superconductor. Thus the susceptibility (χ) took the ideal value for a perfect diamagnetic material given by equation (1.12).

$$B = \mu_0 (H + M) \tag{1.11}$$

$$\chi = \frac{dM}{dH} = -1 \tag{1.12}$$

The meissner effect is generated by shielding currents which develop on the surface of the sample. These currents flow in a direction such that they create a magnetic

field which opposed the externally applied field. However these currents are not confined to an infinitely thin surface layer, of course, but rather to a finite but small depth below the surface called the London penetration depth *(λ)*. The penetration depth is characteristic of a given material but varies typically between 10-500 nm, for Nb_3Sn it is 124 nm.

For large applied magnetic fields applied to a sample while it is below T_c a breakdown in the Messiner effect is observed, and based on the character of this breakdown superconducting materials are classified into two categories. In Type-I superconductors, superconductivity is destroyed abruptly when the applied external field was increased beyond a certain critical value H_c. This is observed in most elemental superconductors like Hg, Pb, V etc. In a Type-II superconductor, an increase in magnetic field beyond a certain critical value H_{c1} results in the penetration of the magnetic fluxons. This is called the mixed state. Further increase in magnetic field beyond a certain critical value H_{c2} results in superconductivity being destroyed in these materials. Most compound superconductors such as intermetallics and alloys are Type-II superconductors. The magnetization curves for ideal Type-I and Type-II superconductors are shown in Figure 1.4; Figure 1.5 shows the magnetic field-temperature phase space for theses superconductors.

An important parameter describing this classification into Type-I and Type-II superconductors is the Ginzberg-Landau parameter *(κ)* given by equation (1.13). Here λ is the penetration depth while ξ is the coherence length defined as the distance over which an appreciable change in the density of superconducting electrons can occur. This was

shown to be equivalent to the spacing between the cooper pair of electrons by the BCS theory proposed by Bardeen, Cooper and Schrieffer [19].

$$\kappa = \frac{\lambda}{\xi} \tag{1.13}$$

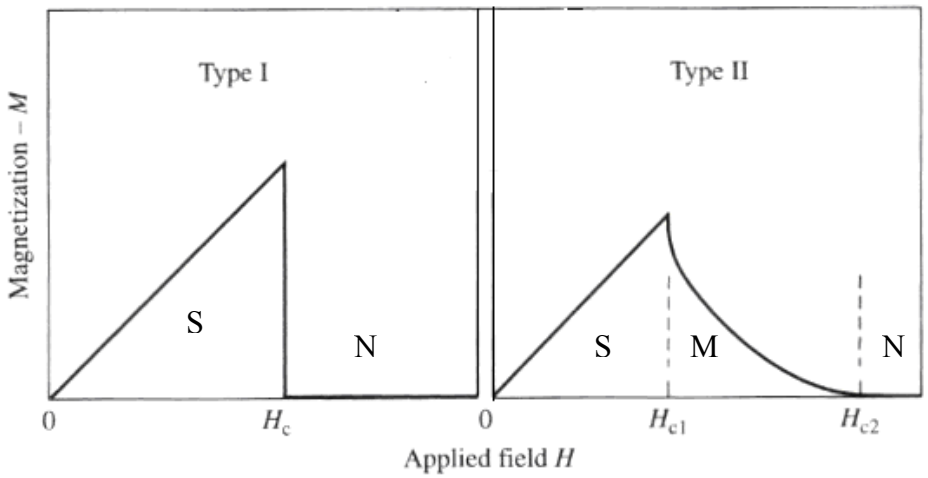

Figure 1.4 Variation in magnetization due to the applied field in Type-I and Type-II superconductors. ((S) - Superconducting, (M) - Mixed state, (N) - Normal state) [15].

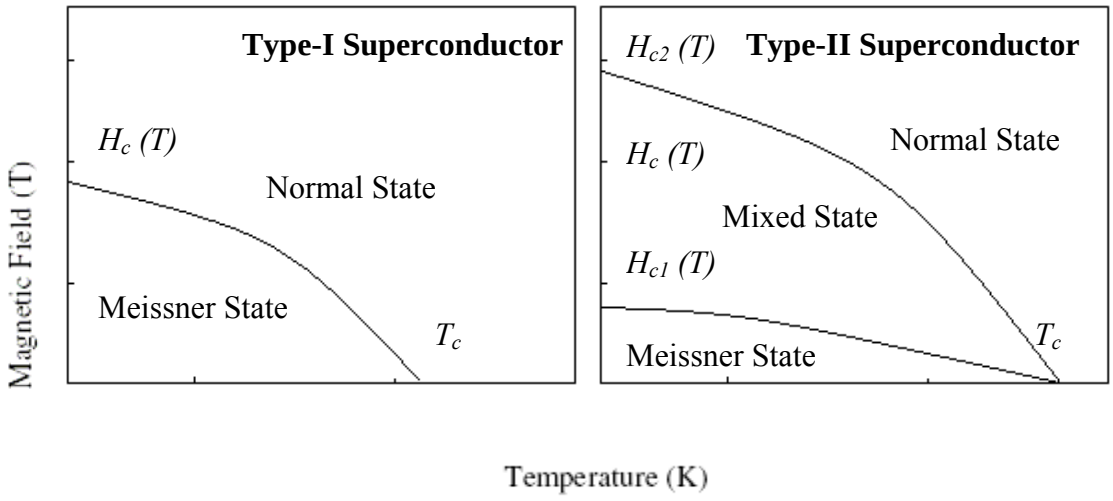

Figure 1.5 The field- temperature space for a Type-I and Type –II superconductor.

$$E_S \approx \frac{1}{2}\mu_0 H_C^2(\xi - \lambda) \tag{1.14}$$

The surface energy per unit area of the boundary between the normal and the superconducting region can be given by equation (1.14). Ginzberg-Landau parameter $\kappa < 1$ are defined as Type-I superconductors. This corresponds to a positive surface energy between the normal and superconducting regions, thus energetically preventing the formation of normal regions within the superconductor below critical fields H_c. A Ginzberg-Landau parameter $\kappa > 1$ defines Type-II superconductors and is associated with a negative surface energy between the normal and superconducting regions. This makes it energetically favorable for normal regions to be present within the superconductor and represents the mixed state in theses superconductors. Thus above the lower critical field H_{c1} discrete quant of magnetic flux called fluxons are observed to penetrate the superconductor. The movement of these fluxons results in energy losses within the material. This can be prevented by material imperfections such as grain boundaries, solute atoms, dislocations etc. which are primarily responsible in pinning the fluxons with a flux pinning force (f_p) and aid in loss free current transport.

CHAPTER 2

Nb_3Sn SUPERCONDUCTORS

2.1 Nb_3Sn – Crystal structure and Critical Parameters

Nb_3Sn is a brittle intermetallic compound having the A15 crystal structure. It is a Type-II superconductor and belongs to the *Pm-3n* space group. The generic formula for the A15 crystal structure is A_3B, where the B atoms are found to occupy the body centered atom positions within the lattice with two A atoms on each face as shown in Figure 2.1. In most A15 compounds, A atoms are occupied by transition elements such as (Nb or V) and B atoms are usually group III or group IV elements (Sn, Ge, Ga or Al) [20].

Nb_3Sn is thermodynamically stable over the composition range ~18 to ~25 at% Sn. It undergoes a cubic to tetragonal transitions at temperatures below 43 K [21-22] but only at Sn compositions greater than 24.5 at% Sn [8]. The lattice parameter of the A15 is 0.529 nm at the stoichiometric composition while the spacing between the Nb atoms in the A15 is around 0.265 nm which is less than that in elemental Nb (0.290 nm) [8]. This results in an increase in the density of states and in turn better superconducting properties than *bcc* Nb [21].

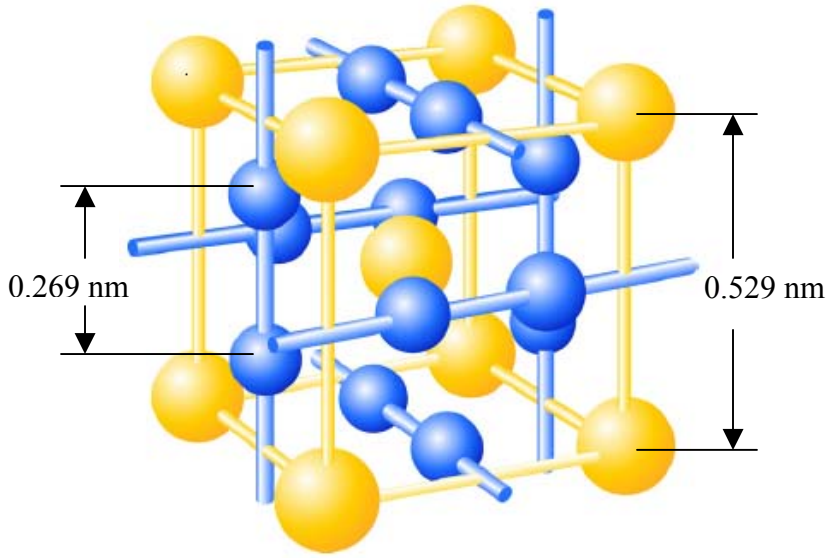

Figure 2.1 A15 crystal structure of Nb_3Sn, the Sn atoms (B) occupy *bcc* lattice sites while the Nb atoms (A) are in the form of orthogonal chains through the face centers [21].

Superconducting transition temperature T_c (K)	17.8 ±0.1
Upper critical field $Hc_2(0)$ (T)	25 ± 0.5
Lower critical field $Hc_1(0)$ (T)	0.038
Martensitic transformation temperature T_m (K)	40 ~ 45
Room temperature lattice parameter a (Å)	5.293 ± 0.001
Tetragonal distortion (a/c)	1.0026 ±0.0001
London penetration depth λ (Å)	1240
Coherence length ξ (Å)	36
Ginzberg-Landau parameter (κ)	34

Table 2.1 Critical parameters of Nb_3Sn [23]

The superconducting properties T_c and B_{c2} are also strongly related to the atomic Sn contents in the A15 as shown in Figure 2.2. The critical temperature was found to increase with increasing Sn content while the critical field was initially found to increase at lower Sn contents and later decrease at Sn contents greater than 24.5 at% due to the martensitic transformation. Table 2.1 gives the characteristic parameters of Nb_3Sn which was taken from the work of Guritanu *et. al.* [23].

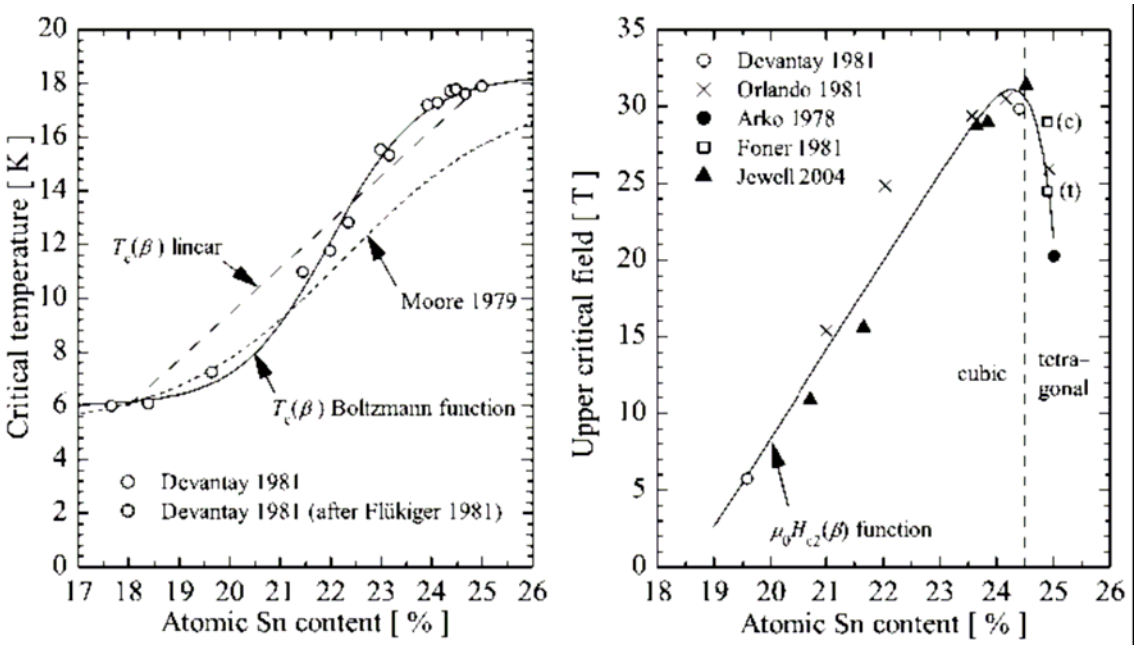

Figure 2.2 Variation of the critical temperature and upper critical field with atomic Sn content (reproduced from the work of A. Godeke [21]).

2.2 The Nb-Sn phase Diagram and Nb_3Sn formation routes

The Nb-Sn binary phase diagram that was determined by Charlesworth *et. al.* [24] in 1970 is shown in Figure 2.3. From this phase diagram it can be realized that when *bcc* Nb is alloyed with Sn it can form three intermetallic compounds namely $NbSn_2$, Nb_6Sn_5

and Nb_3Sn. While $NbSn_2$ and Nb_6Sn_5 are line compounds, the Nb_3Sn phase exists in the form of a solid solution and is stable over a range of composition from ~18 to ~25 at% Sn. As discussed earlier, Nb_3Sn is the superconducting phase with superior properties found close to the stoichiometric composition while the $NbSn_2$ and Nb_6Sn_5 are non-superconducting at liquid helium temperature and are of little commercial interest. Hence our main aim in the manufacture of these composites is to maximize the fraction of the Nb_3Sn phase.

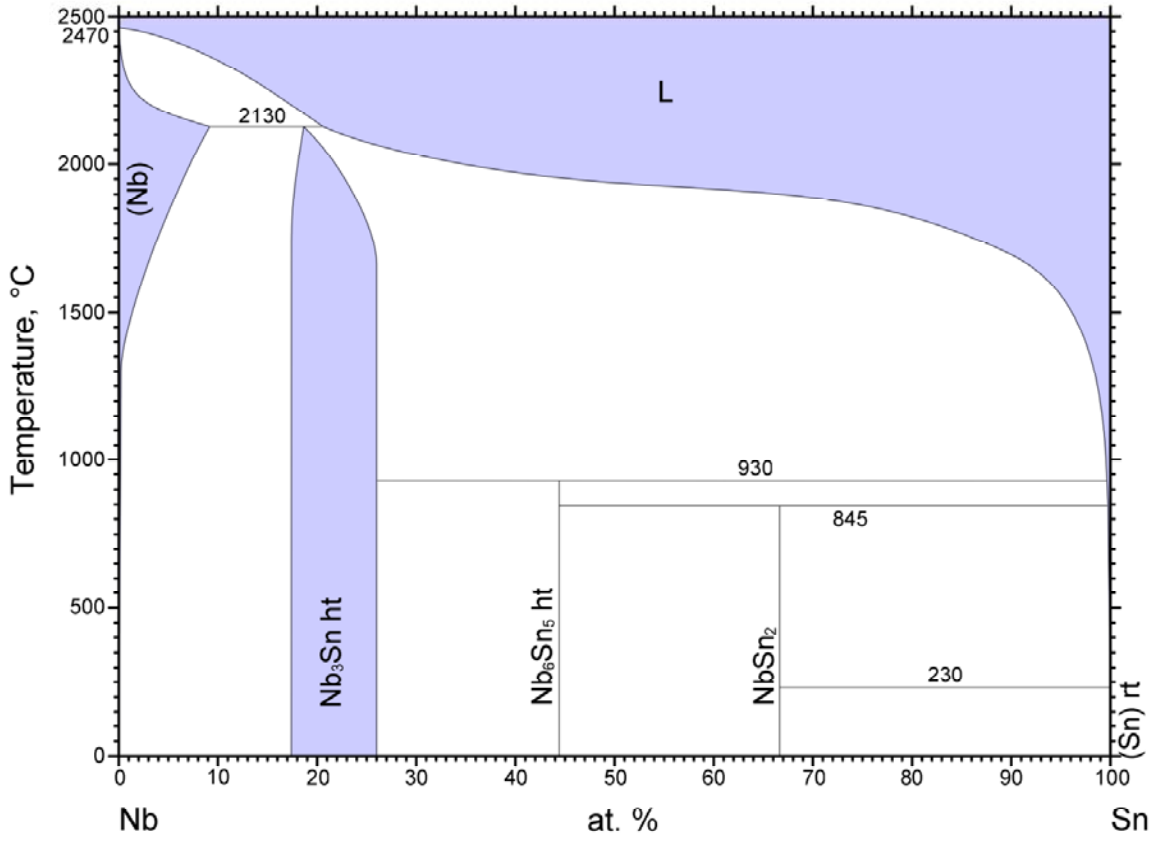

Figure 2.3 Nb-Sn binary phase diagram determined by Charlesworth *et. al.* [24] (Reprinted with permission of ASM international)

Recent work on the Nb-Sn binary phase diagram by Okamoto [25] has shown that the Nb_6Sn_5 phase to be stable above 739°C, unlike the diagram of Charlesworth who claimed that the Nb_6Sn_5 phase was stable at room temperature. Moreover the solubility of Sn in Nb at lower temperatures (below 800°C) was also much higher. Also according to this phase diagram Nb_3Sn exists in the form of a line compound at room temperature however at elevated temperatures it does have a solubility range (25-27 at% Sn at 600°C). In the present work the Nb-Sn phase diagram determined by Charlesworth has been followed as it is the generally accepted phase diagram in literature and is more consistent with the obtained results.

Nb_3Sn strands have been manufactured successfully by a number of different methods; the bronze, internal-Sn (RRP) and powder-in-tube (PIT) routes. The A15 phase in all the above methods is obtained by reactive diffusion, of course, typically in the presence of Cu at temperatures between 650-725°C. However, the tube-type and PIT conductors are fundamentally different from the internal-Sn and bronze conductors because the former use diffusion between Nb and a Sn rich alloy, while internal-Sn and bronze conductors employ a Cu-rich bronze alloy. Figure 2.4 shows the Cu-Nb-Sn phase diagram at 675°C determined by W.L.Neijmeijer in 1987 [26]. The diagram shows a number of three phase regions some of which are $NbSn_2$-Nb_6Sn_5-L, Nb_6Sn_5-Cu_3Sn-L and Nb_6Sn_5-Nb_3Sn-Cu_3Sn. Also marked on this diagram are the reaction sequences for the composites discussed above. A Cu-Sn starting source with Sn contents in the Cu-rich part of the ternary diagram (certainly less than 27 at%) as in the case of the bronze route and internal-Sn conductors form the A15 directly from the Cu-Sn Nb interface. On the other

hand intermetallic-based PIT conductors use $NbSn_2$ powders in combination with Cu resulting in a Sn-rich phase up against the Nb and lead to formation of the A15 via an intermediary Nb_6Sn_5 phase [26-29]. Some other interesting variants of the intermetallic-based PIT conductors have been proposed, including work by Tachikawa et al. [30], where Nb_6Sn_5 was used directly instead of beginning with $NbSn_2$.

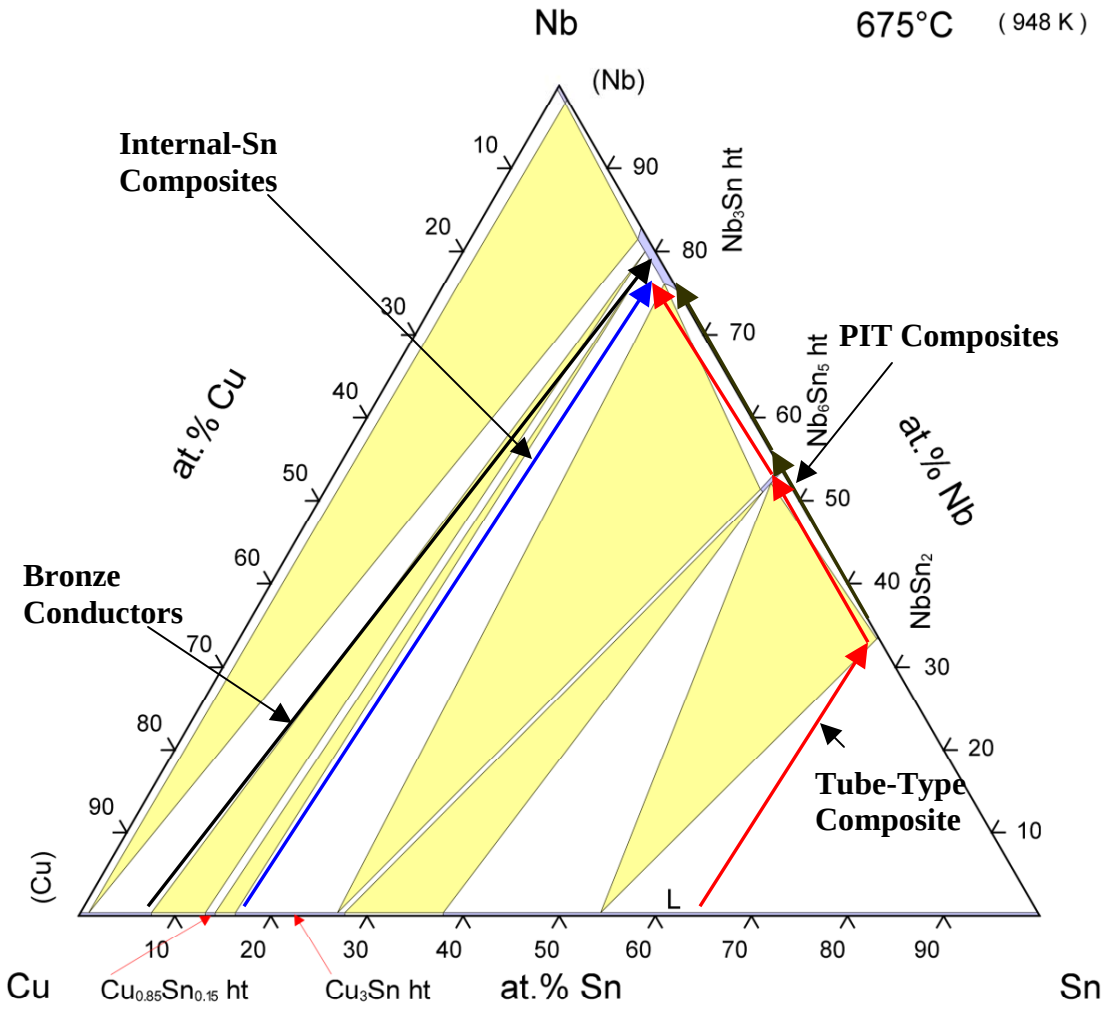

Figure 2.4 Cu-Nb-Sn ternary phase diagram at 675°C [26], the reaction routes for the various types of Nb_3Sn composites have also been indicated (Reprinted with permission of ASM international)

Tube-type composites have some similarities to PIT type superconductors [29, 31]. For Sn-rich Cu-Sn alloys with typical reaction temperatures of 650-700°C a Sn rich bronze liquid phase forms up against the Nb tube wall followed by subsequent diffusion of Sn atoms through the Nb [32], as might be expected from the binary phase diagram [24]. If the Sn content of the source (Cu-Sn alloy) is more than 55 at%, $NbSn_2$ is first formed, followed by Nb_6Sn_5. On the other hand if the Sn content is between 27 at% and 55 at% Nb_6Sn_5 forms directly (at 675°C) and the A15 is formed from the Nb_6Sn_5. At longer reaction times when the Sn in the core drops below 27 at%, Nb_6Sn_5 formation stops and fine grain A15 grows on the outer boundary of the Nb_6Sn_5 by Sn diffusion into the Nb layer surrounding it. At the same time, this Sn depletion in the Nb_6Sn_5 layer causes it to convert to coarse grain A15. The main aim in these composites was to maximize the fine grain A15 fraction and reduced the coarse grain A15 fraction by suppressing the growth of Nb_6Sn_5. Some authors have attempted to destabilize the Nb_6Sn_5 phase by alloying and prevent the formation of coarse grain A15 with little success [26].

2.3 Ternary additions to the A15

2.3.1 Copper addition

Copper is generally added in its elemental form in internal-Sn conductors, PIT strand as well as tube-type conductors; however it was initially used in the form of bronze alloy. The main role of Cu in these composites is to form Cu-Sn phases which act

as a Sn source to form the A15. The main advantage of adding Cu is it acts as a catalyst and enables the A15 formation at lower reaction temperatures thus limiting grain growth and in turn improving the critical current density. It has also been found that the presence of Cu destabilizes line compounds such as $NbSn_2$ and Nb_6Sn_5 during A15 formation [33]. Although from the Cu-Nb-Sn ternary phase diagram it can be realized that the solubility of Cu in the A15 at 675°C is around 1.7 at%, work done by M. Suenaga shows that at room temperature it mainly exists at grain boundaries [34-35]. The effect of Cu on the superconducting properties of the A15 is not quite clear. Recent work suggests that the presence of Cu has reduced B_{c2} [36].

2.3.2 Titanium and Tantalum additions

Ternary additions such as Ta and Ti are added mainly to improve the superconducting properties of the A15 phase. While Ta is usually added as an alloying addition in the Nb filament, Ti is added in several different ways, the most common of which is in the form of a Sn-Ti alloy. Both Ti and Ta occupy Nb sites in the A15 lattice and have been found to suppress the cubic to martenstic transformation for Ta > 2.8 at % and Ti > 1.3 at% [37]. Retention of the cubic phase results in an increase in B_{c2}. Both Ta and Ti have been found to increase the normal-state resistivity and in turn increase B_{c2} [37]. Also Ti increases the layer growth rate, thereby forming A15 at smaller reaction times suppressing grain growth [38]. Extensive work has also been performed on the simultaneous addition of Ta and Ti to internal-Sn strands [38]. It was observed that the kinetics of the A15 formation was enhanced by the presence of Ti and Ta however no increase in B_{c2} was observed due to the additions.

2.4 Multifilament Manufacturing Processes

2.4.1 The Bronze Process

The bronze process was perhaps the first multifilamentary wire fabrication technique. In it the A15 is formed via a solid state diffusion reaction between Nb and an α-bronze matrix [39]. In this process thin ductile Nb or Nb-(Ti or Ta) filaments are placed in an α-bronze matrix to form the subelement. These are then restacked in a Cu matrix and the billet is extruded and drawn to the final required dimensions. The subelements needed to be surrounded by Nb or Ta barriers to prevent contamination of the Cu matrix with Sn during A15 formation. Figure 2.5 shows a cross section of a strand fabricated by the bronze route.

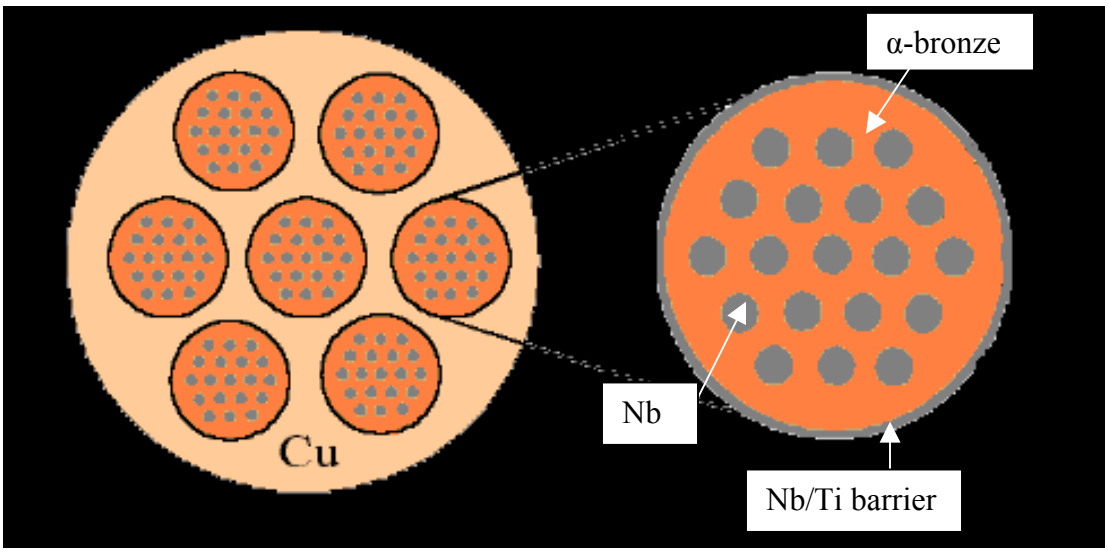

Figure 2.5 Cross section of the wire along with a subelement obtained by the bronze route [28].

Frequent annealing steps are required as a result of work hardening in the bronze matrix, which increased the cost of manufacture of these strands. However, the main drawback is the low Sn levels and large gradient observed across the A15 due to low Sn contents in the α-bronze matrix [21]. This leads to relatively low properties for many applications.

2.4.2 The Internal-Sn Process

The internal-Sn process was developed to overcome limitations of the bronze process. In theses strands a subelement consisted of a central Sn core surrounded by a Cu matrix embedded with Nb filaments as shown in Figure 2.6. These subelements are also surrounded by a diffusion barrier of Nb or Ta on the outside. During heat treatment the Sn atoms from the core diffuse through the Cu matrix and react with the Nb forming the A15 similar to the bronze conductors. The main advantage in this process is the higher initial Sn/Cu ratio than the bronze route resulting in superior quality A15. Also annealing is not required during fabrication.

The process has a number of drawbacks, for example, the longer reaction times due to the multiple pre-reaction holds at lower temperatures (around 200°C and 400°C) needed to form homogenous Cu-Sn phases prior to A15 formation. The ramp rates used during heating are relatively low too. Also the manufacturing process is expensive as the strands are hot extruded. Another major drawback is the filament interconnection or bridging during A15 formation which results in larger hysteresis losses in these strands.

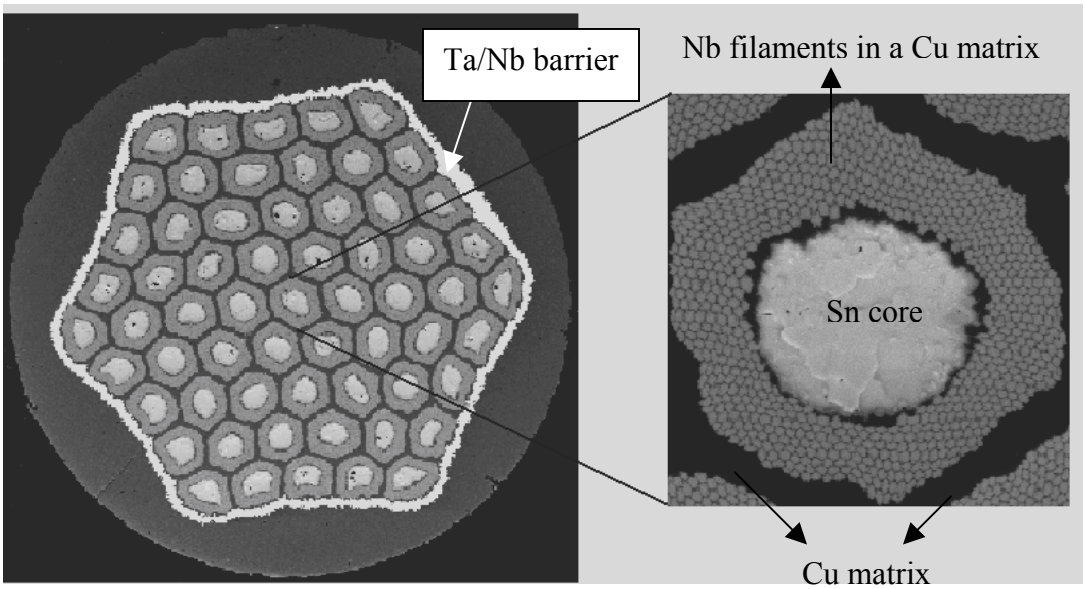

Figure 2.6 SEM-BSE micrograph of the cross section of the wire obtained by the internal Sn route.

2.4.3 The Powder in Tube Process

Powder in tube composites were initially developed by the Netherlands Research Foundation (also called the ECN process). It consists of subelements of Nb with a central core containing $NbSn_2$ powder with additions such as Cu [26-31, 40-42]. Figure 2.7 shows a cross section of theses composites.

The main advantages of this process is the large Sn content of the core, simple design and lower heat treatment time as pre-reaction anneals are not required. This results in A15 with higher Sn contents, a fine grain size, and in turn better superconducting properties. However the main drawbacks of this process are a lack of ductility of the powder core making wire drawing difficult and resulting inhomogeneities in the strands.

In addition control over the powder size is expensive but essential in obtaining better properties and superior conductors that do not rupture while drawing.

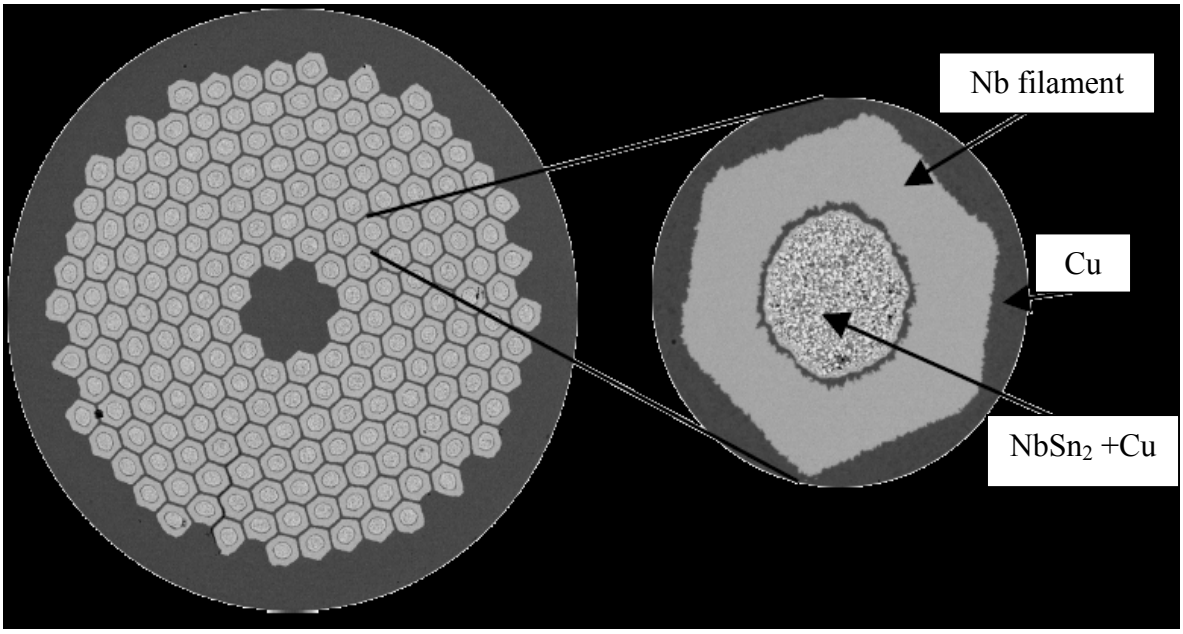

Figure 2.7 Shows the cross section of a PIT strand [38].

2.4.4 The Tube-Type Process

As discussed earlier, tube-type composites have some similarities to PIT type superconductors, however in these composites the $NbSn_2$ powder core is replaced by pure Sn metal surrounded by a thin tube of elemental Cu and is as shown in Figure 2.8. During heat treatment the A15 forms via the $NbSn_2$ and Nb_6Sn_5 route by a liquid state diffusion reaction between the Nb filament and the Sn rich Cu-Sn alloy [43-44]. These composites have all the above mentioned advantages of PIT strands [45] along with an easier and cheaper fabrication process (wire drawing) due to the ductile Sn core.

The general idea of "tube-type conductors" where Cu and Sn are inserted into Nb tubes has been pursued before as the solid-liquid diffusion process [46-52]. Early on, geometrically similar conductors were fabricated by Murase and associates [46]. The phase formation sequence was presumably similar to the present case, but no details are available, making identification of the cause of the substantially lower transport values difficult to asses.

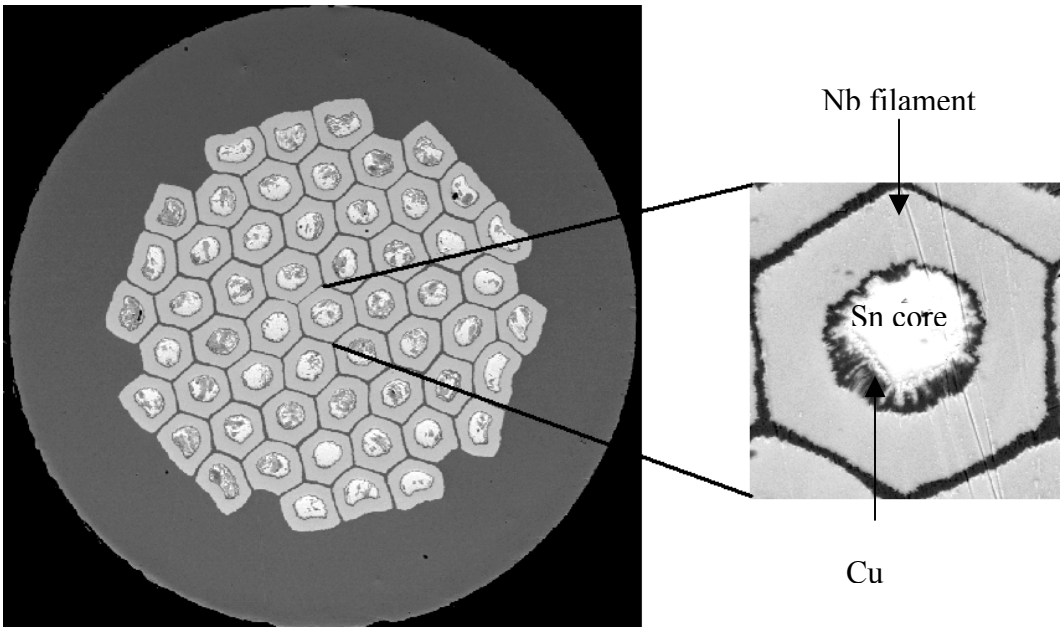

Figure 2.8 SEM-BSE image of the cross section of the wire fabricated by the tube-type process.

More recently several other groups have studied geometrically similar conductors, including Rodrigez [47] and Yamasaki [48, 51]. The conductor described in [47] has 271 filaments, and has a J_c of 680 A/mm^2 at 10 T. The conductors described by Yamasaki

[48] reach J_cs in the A15 of 6000 A/mm^2 at 9.5 T in 37 filament conductors, and have similar A15 formation rates (≈ 5 μm after 650°C/50 h) which varied with filament diameter. The conductors described in Chapter 3, and also in [32] presently reach a non-Cu J_c of 2300 A/mm^2 at 12 T in 169 filaments, and d_{eff} values reaching as low as 33 μm [53].

CHAPTER 3

EXPERIMENTAL PROCEDURES AND MEASUREMENT TECHNIQUES

3.1 Sample Specifications

The five strands (S1 to S5) used in this investigation are described in Table 3.1. These strands were manufactured by the wire drawing process at Hypertech Research Inc. in Columbus, Ohio. The strands had an outer diameter of 0.75 mm; however they had various designs and filament counts ranging from 61-169. Also the filament size varied from 60 microns in strand S1 to about 30 microns in strand S4. In order to facilitate this study the subelement Nb/Sn area ratio was kept constant around 2.5, while the Sn/Cu ratio varied from about 3.3 to 7.5. Back scatter electron images of the cross sections of the five unreacted strands are as shown in Figure 3.1. Figure 3.2 shows a SEM-BSE image of a subelement in strand S1 prior to reaction, the unreacted subelement consisted of a central Sn core surrounded by a Cu tube with a coaxial hexagonal filament of Nb-7.5 wt% Ta. The Cu, Sn, Nb, and non-Cu areas were determined by image analysis on fully deformed but unreacted strands using software packages such as Image tool and the Clemex image analyzer.

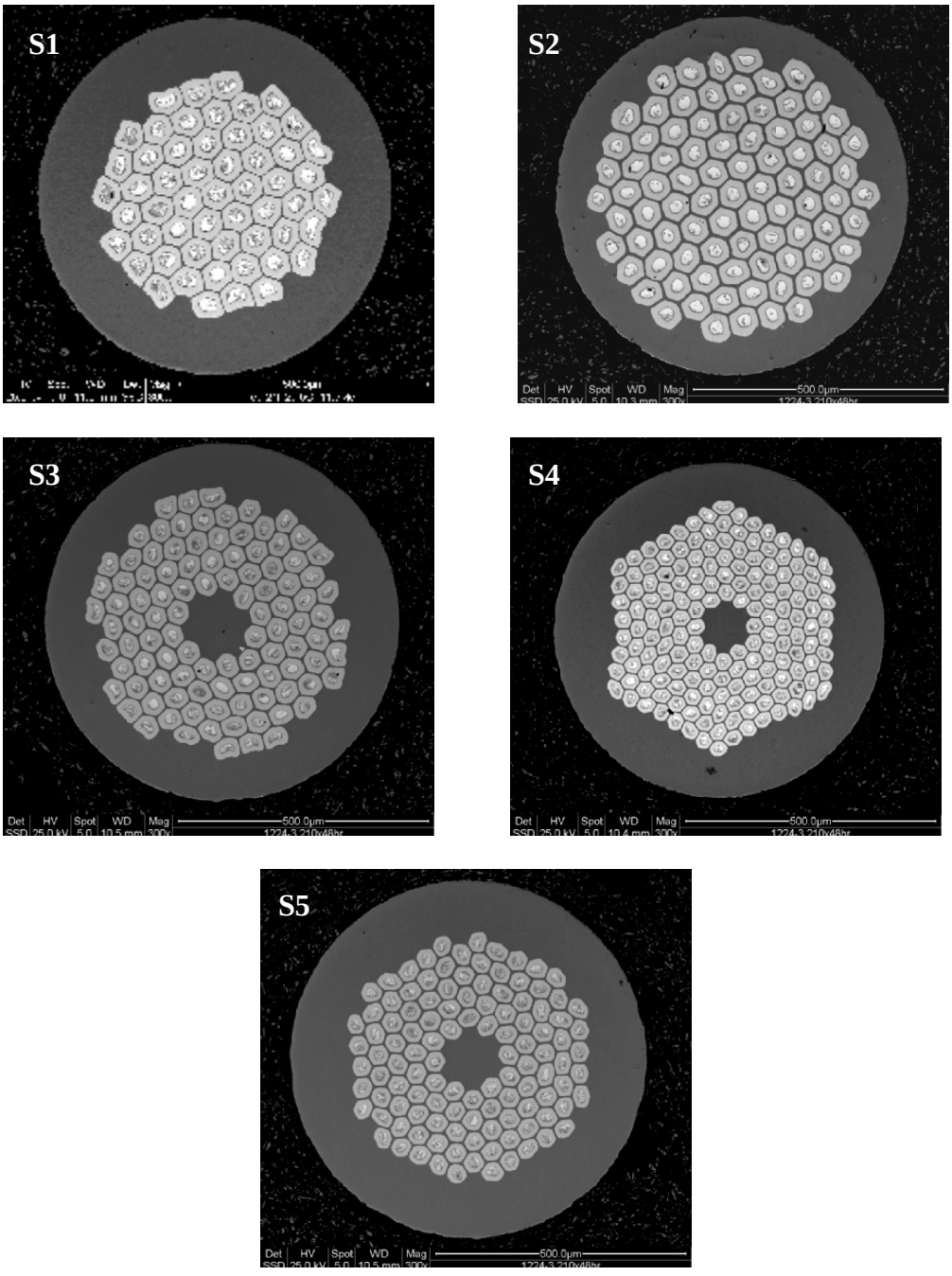

Figure 3.1 SEM-BSE images of the cross section for the five unreacted strands (S1 to S5), each having a diameter of 0.75 mm and subelements ranging from about 61-169.

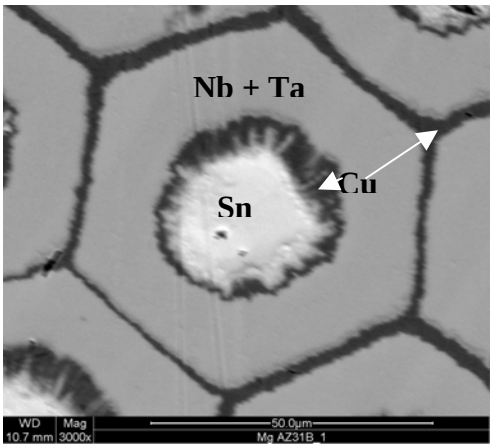

Figure 3.2 SEM-BSE micrographs of an unreacted subelement in strand S1 [44].

Strand Name	S1	S2	S3	S4	S5
Filament Count (Restack)	61	91	127	169	169
Subelement Radius (µm)	28.5	23.8	20.6	15.3	17.9
Copper Area % (Sub)	7.9	6.1	4.9	4.4	3.7
Tin Area % (Sub)	26.2	26.4	26.9	27.7	27.9
Niobium Area % (Sub)	65.9	67.5	68.2	67.9	68.4
Nb/Sn Area Ratio (Sub)	2.5	2.6	2.5	2.4	2.4
Sn/Cu Area Ratio (Sub)	3.3	4.3	5.5	6.3	7.5
At% Sn	62.0	68.2	72.4	75.2	77.9

Table 3.1 Strand Specifications.

3.2 Heat Treatment

In order to form the A15 phase samples were subjected to heat treatment at elevated temperatures ranging from 650-800°C. The heat treatment parameters varied

depending on the purpose of investigation. Table 3.2 describes the heat treatment schedules for strands S1 and S4 that were used to investigate phase evolution leading to A15 formation as a function of reaction time. Table 3.3 describes heat treatment schedules for samples heat treated to ensure complete reaction. These samples were investigated to obtain experimental data for the analytical model as well as for compositional and microstructural analysis.

Heat treated samples were 25 cm in lengths with ends sealed to avoid Sn leakage at elevated temperatures. They were pre-cleaned using ethyl alcohol and encapsulated in quartz tubes (ID = 0.8 cm) under an argon atmosphere of 200 torr. They were then subjected to heat treatment in a tube furnace interfaced to a computer with a temperature control of +/- 2°C. The ramp rates used for all heat treatments were 50°C/h. Following heat treatment the samples were quenched in a water tank to arrest the high temperature reaction.

Strand Name	Billet Name	HT (C/h)	Non-Cu %
S1	T1026	650,725/1,2,4,8,16,32,64, 128,250	29.5%
S4	T1162	650,725/1,2,4,8,16,32,64, 128,250	35.5%

Table 3.2 Heat treatment schedules for phase evolution.

Strand Name	Billet Name	HT (C/h)	Transport HT (C/h)	B_{c2} HT (C/h)	Non-Cu %
S1	T1026	650,675,700,725,800/ 250	675/108	675,725/ 250	29.5%
S2	T1102	650,675,700,725,800/ 250	675/60	675,725/ 250	51.5%
S3	T1135	650,675,700,725,800/ 250	675/72	675,725/ 250	37.5%
S4	T1162	650,675,700,725,800/ 250	675/48	675,725/ 250	35.5%
S5	T1204	650,675,700,725,800/ 250	675/60	675,725/ 250	32.5%

Table 3.3 Heat treatment schedules for complete reaction, transport and B_{c2} measurements.

3.3 Metallographic Sample Preparation for Electron Microscopy

Samples for electron microscopy were extracted from the central portions of the reacted strands. Two kinds of molds were used for mounting; cold mounting for unreacted strands and hot mounting for the reacted ones. With the cold mounting technique stainless steel clips were use to keep the samples vertical and a mixture of epoxy, hardener and carbon power in the ratio 4:1:5 was used to form the mold. The mold was then left to cure in air for about 6 hours. With the hot mounting technique samples were soldered onto a copper block then sectioned and conductive Bakelite powder was used to form the mold. Hot isostatic pressing technique was used to sinter the powder together.

The mounted samples were metallographically polished using silicon carbide abrasive papers starting from 300 grit size up to 1200. They were then cleaned in ethyl alcohol using ultrasonic cleaning. Later they were mounted in stainless steel grips and polished for 6-10 hours in a vibratory polishing machine on one micron cloth using a silica gel colloidal solution. Prior to SEM analysis, final cleaning was done ultrasonically and then baked in an oven at 70°C for an hour. Fracture SEM samples were prepared by the etching technique in which samples were etched using a mixture of 0.1 N nitric acid for about 60 seconds. This was done to etch away the matrix Cu and obtain a brittle fracture surface for grain size analysis.

3.4 J_c and B_{c2} Measurements

The critical current density (J_c) as well as upper critical magnetic field (B_{c2}) was measured using the four point technique [54] shown schematically in Figure 3.3. In this technique a pair of twisted leads from the voltmeter was connected directly across the central portions of the sample while a separate pair of leads was used to pass current through the sample. The voltage measured by the voltmeter is given by equation (3.40) where I was the current through the sample and ε the current through the voltmeter. Since the resistance of the voltmeter was typically higher than any other resistances in the circuit this equation could be approximated to equation (3.41). The main advantage of the four point technique over the two point technique for cryogenic transport measurements was that the voltage readings did not include the effects of contact resistance as well as the resistances of the connecting leads.

$$V = (I - \varepsilon)(R_{Sample}) - \varepsilon(2R_{contact} + 2R_{lead}) \tag{3.40}$$

$$V = IR_{sample} \quad (\text{As } \varepsilon \rightarrow 0) \tag{3.41}$$

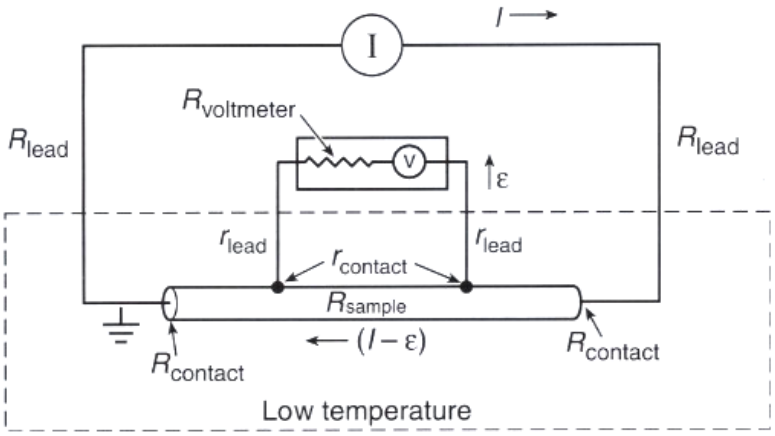

Figure 3.3 Shows the schematic sketch of the circuit diagram used in the four point technique [54].

Critical current density (J_c) was measured by the "ITER-barrel" technique using the wind and react protocol. The ITER is a helically grooved tube having a 3.2 cm bore made up of Ti-6Al-4V alloy whose ends were press fitted to Cu rings. The unreacted wire was wound along the grooves under tension and was fixed by screws in the Cu end rings as shown in Figure 3.4a. The barrel was then heat treated in an inert atmosphere of argon. Prior to measurements the ends of the wire were soldered onto the Cu end rings using Pb-Sn solder after which the barrel was mounted on the measuring probe made out of a Cu rod. Care was taken to ensure that the barrel was well soldered to the probe in order to minimize the contact resistance. The voltage tabs were soldered onto the sample with a

gauge length of 50 cm between the tabs shown in Figure 3.4b. The probe along with the barrel was then pre-cooled in a liquid N_2 dewar.

The cryostat used for measuring J_c consisted of a vacuum insulated cylindrical bore with a superconducting magnet made out of hybrid NbTi/Nb_3Sn windings at the bottom. The probe was inserted into the central bore of the superconducting magnet and immersed in liquid helium temperature. The current leads from the power supply were externally connected to the probe. The superconducting magnet was ramped up to 14 T and the voltage across the gauge length was measured as a function of current as the magnetic field was reduced from 15 T to 10 T. With the aid of the software the critical current I_c was extracted as well as the n-value describing the transition from the superconducting state to the normal state was obtained.

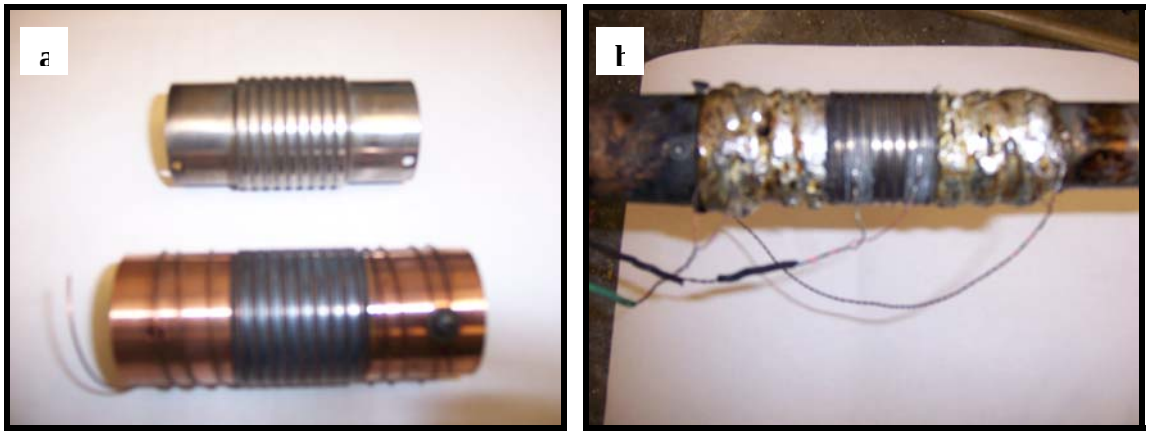

Figure 3.4 a) Shows an ITER-barrel on which the unreacted wire was wound over the central Ti-6Al-4V b) Shows the ITER barrel with voltage tabs mounted on the Cu probe.

Upper Critical Field (B_{c2}) measurements were conducted at National High Magnetic Field Laboratory (NHMFL) in Tallahassee Florida, using the four point

technique discussed earlier on samples which were 10 mm long. The voltage tabs were attached to the central portion of the sample with a gauge length of 5 mm using Pb-Sn solder. The upper critical field was measured by passing a small current trough the sample and measuring the resistance across the gauge length in a varying magnetic field. The measurements were performed at 4.2 K and the magnetic field ranged from 0 to 33 T. Currents of, 10 mA were used with a DC current reversal, and fields up to 30 T were applied transversely to the sample using the DC resistive magnet. The variation of resistance with upper critical field is as shown in Figure 5.12. Both the 0.1 and 0.9 transitions were extracted from these curves with the aid of software.

3.5 Scanning Electron Microscopy and Energy Dispersive X-Ray Spectroscopy

In the scanning electron microscope a high energy beam of electrons from the source (in the form of a filament or field emission gun) is directed towards the surface of the sample. Figure 3.5 shows the schematic sketch of the signals generated as a result of the electron beam sample interaction with a bulk sample. It consists mainly of Secondary electrons, Backscattered electrons and Characteristic X-rays [55-56].

Secondary electrons are the electrons that escape from the surface of the specimen with energies below 50 eV. They are detected using a scintillator photomultiplier system called the Everhart-Thornley detector and are used mainly in the analyses of fracture surfaces and surface defects. Theses electrons having a low energy are accelerated towards the detector with the aid of a small positive bias. Backscattered electrons consist of high energy electrons that are reflected back from the interaction volume (the region into which the electrons penetrate in the sample). The brightness of the backscattered

electrons tends to increase with increasing atomic number and is mainly used in phase analyses. These electrons can be detected using scintillator or solid state detectors located above the specimen with a central annulus through which the incident beam passes through.

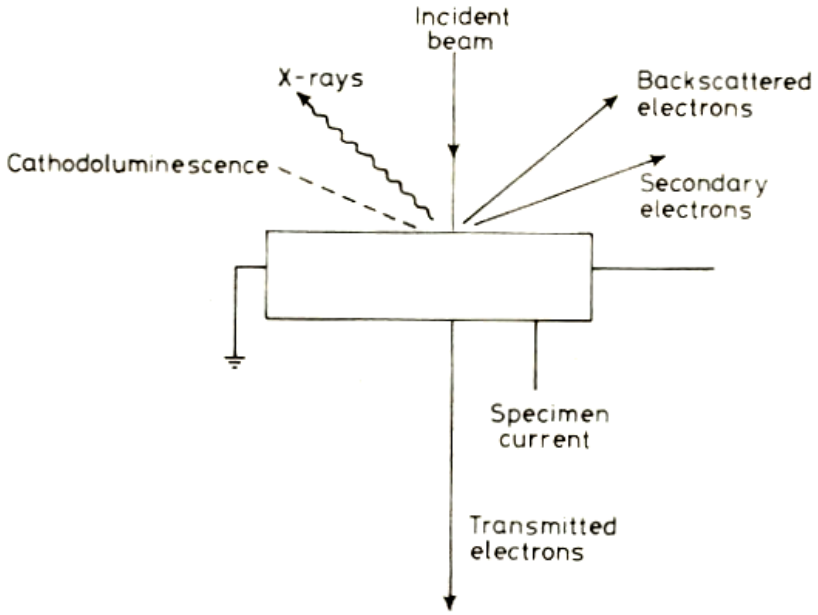

Figure 3.5 shows the schematic sketch of the signals generated as a result of the electron beam sample interaction [55].

Energy Dispersive X-ray Spectroscopy is a quantitative method mainly used in chemical analysis of a specimen by analyzing the Characteristic X-Rays produced [56]. When a high energy beam of electrons is incident on a sample it tends to knock of some of the electrons from the inner shell in the atom leaving it in the excited state. The

vacancy is soon occupied by one of the outer electrons emitting energy in the process. This energy is in the form of radiation having a definite wavelength and is called characteristic radiation. The EDS detector should be calibrated prior to measurements with a standard sample of known composition. Typical EDS profiles are shown in Figure 5.2 which consists of a graph of intensity versus energy in eV. In order to analyze a given region of the specimen the interaction volume should be controlled by adjusting the accelerating voltage.

In this work backscattered electron micrographs were obtained using the FEI QUANTA 200SEM and the ESEM both having a spatial resolution of 100 nm at 5 kV. Microchemical analysis was performed via Energy Dispersive spectroscopy (EDS) on the ESEM at 15kV and an operating distance of 11 mm. A standard homogenous bulk sample was used for calibration [57]. Interaction volume was calculated using Monte Carlo simulations and was kept below 1.6 micron [58]. Fractography was performed on samples with the aid of the SIRION (using a field emission gun (FESEM)) having a spatial resolution of 2.5 nm at 5 kV operating in the ultra high resolution mode.

CHAPTER 4

EFFECT OF HEAT TREATMENT AND INITIAL SUBELEMENT Sn/Cu RATIO ON THE INTERDIFFUSION MICROSTRUCTURE

4.1 Introduction

In this chapter multifilamentary tube type composites consisting of subelements of Nb-7.5wt% Ta with initial subelement Sn/Cu ratios from about 3.3 to 7.5, as given in Table 3.1, were studied in terms of their phase evolution and reaction systematics. Microstructural evolution was investigated at different time intervals during the heat treatment in an attempt to determine the factors affecting growth of the fine and coarse grain regions of A15. A detailed analysis of layer growth rates was carried out to optimize the heat treatment as a function of reaction temperatures, subelement Sn/Cu ratios, and Nb-tube thicknesses (varying subelement sizes for tube conductors). The results were compared to the growth rates in PIT and internal-Sn strands. Moreover an analytical model was discussed, to aid in predicting the ratio of fine to coarse grain A15 for varying subelement Sn/Cu ratios formed after complete reaction. The predictions were compared with the experimentally obtained data.

4.2 Phase Evolution leading to A15 Formation

Microstructural phase evolution was examined for samples of strand types S1 and S4 heat treated at 650°C and 725°C for varying times, in an attempt to determine the effects of the initial subelement Sn/Cu ratio and temperature. Once reacted, the resulting samples were prepared by metallographic techniques and then observed with an SEM in Back Scatter Electron (BSE) mode, and phase identification was performed by Electron Dispersive X-Ray Spectroscopy.

Micrographs for a typical filament of strand type S1 (filaments ~60μm in diameter) are as shown in Figures 4.1(a-f) and 4.2(a-d) after various reaction times at 650°C and 725°C. An SEM image (Figure 4.1(a, b)), taken one hour into the reaction at 650°C indicated that the Cu-Sn liquid which formed on heating had reacted with the surrounding Nb tube to form equiaxed grains of the $NbSn_2$ phase. This phase was also surrounded on its outer periphery by a thin layer of the columnar Nb_6Sn_5 phase. At this point the Sn content of the Cu-Sn source initially containing about 62 at % Sn had dropped below 45 at % Sn indicated by the presence of the Cu_3Sn (dark) as well as the Cu_6Sn_5 (light phases). It was observed that the Nb_6Sn_5 grains were columnar while the $NbSn_2$ grains were equiaxed.

After 8 hours (Figure 4.1(c, d)) the $NbSn_2$ had completely converted to the Nb_6Sn_5 and a thin (several micrometer) layer of the A15 phase had formed on the outer periphery of the Nb_6Sn_5. After 16 hours growth of the Nb_6Sn_5 phase ceased apparently because the Sn content in the core had dropped below the limiting value of ~27 at%, predicted by the Cu-Nb-Sn ternary phase diagram. At this point the Nb_6Sn_5 was

beginning to convert to coarse grain A15, while acting as a Sn source for fine grain A15 formation in the Nb tube which surrounds it. It was also observed that the Nb_6Sn_5 to coarse grain A15 transformation nucleated at the interface between the Nb_6Sn_5 and the fine grain A15. The nucleation and growth of the coarse grain A15 was observed to be strongly controlled by interface effects and it did not grow as a uniform front (Figure 4.2a) as observed in the outward growth of the fine grain A15 and the Nb_6Sn_5.

After about 32 hours (Figure 4.1e) the entire Nb_6Sn_5 region has converted to coarse grain A15 and subsequent to this the growth of the fine grain A15 has decreased significantly, since the Sn source has been extinguished. Figure 4.1f shows the fine and coarse grain A15 after complete transformation in sample S1 heat treated at 650°C for 64 hours. The interface between the coarse and fine grain A15 was observed to contain Kirkendall porosity formed due to Sn diffusing out of the coarse grain region; these voids were occupied by the Cu atoms (Figure 4.3).

A similar phase evolution was observed at 725°C; however the incubation period for the A15 formation was much smaller at this elevated temperature. The incubation period referred to the difference between the initial heat treatment start time and the time at which the fine grain A15 began to form, which was also the time required for the $NbSn_2$ and Nb_6Sn_5 reactions. Moreover the Nb_6Sn_5 front progressed a greater radial distance before converting to coarse grain A15 after about 4 hours (Figure 4.2a). The extended radial growth was primarily due to the shift in the ternary Cu-Nb-Sn phase diagram at 725°C from the values indicated at 675°C, as a result the outward radial growth of the Nb_6Sn_5 continued even though the Sn content in the central core had dropped below the limiting value of ~27 at% Sn at 675°C. The accurate determination of

this limiting value at 725°C was not possible due to the absence of the ternary phase diagram at this temperature, however from the ternary phase diagrams available at 675°C and 800°C it could be approximated to ~23 at% Sn. At about 16 hours the entire Nb_6Sn_5 region had converted into coarse grain A15.

A detailed analysis of phase evolution in PIT composites conducted by W.L.Neijmeijer [26] has some similarities to the ones seen here for tube type conductors. This is to be expected since these conductors start with $NbSn_2$ with Cu additions in a Nb tube, thus a similar transformation to Nb_6Sn_5 and then A15 is expected. There turns out to be practical reasons for avoiding the use of these powders (they can easily cause mechanical problems in wire drawing). However, there are differences as well, including the relative amounts of Sn and Cu in the core and the presence of Nb there. While in principle, it would be possible to vary the Sn to Cu ratio in PIT conductors to investigate the influence of this parameter, to our knowledge this has not appeared in print. Of course this route is quite different from the direct A15 route present for internal-Sn and bronze conductors.

Phase evolution in strand S4 was found to follow a similar pattern to that of strand S1. However, with more Sn in the core larger fractions of $NbSn_2$ and Nb_6Sn_5 were formed and the period of growth for the Nb_6Sn_5 was longer, delaying the onset of A15 formation for a given reaction temperature as compared to that for S1. The smaller Nb_6Sn_5 formation time observed with the higher levels of Sn in the Cu-Sn starting source was also of significant interest, which of course led to initiation of the Nb_6Sn_5 conversion to coarse grain A15 earlier as well.

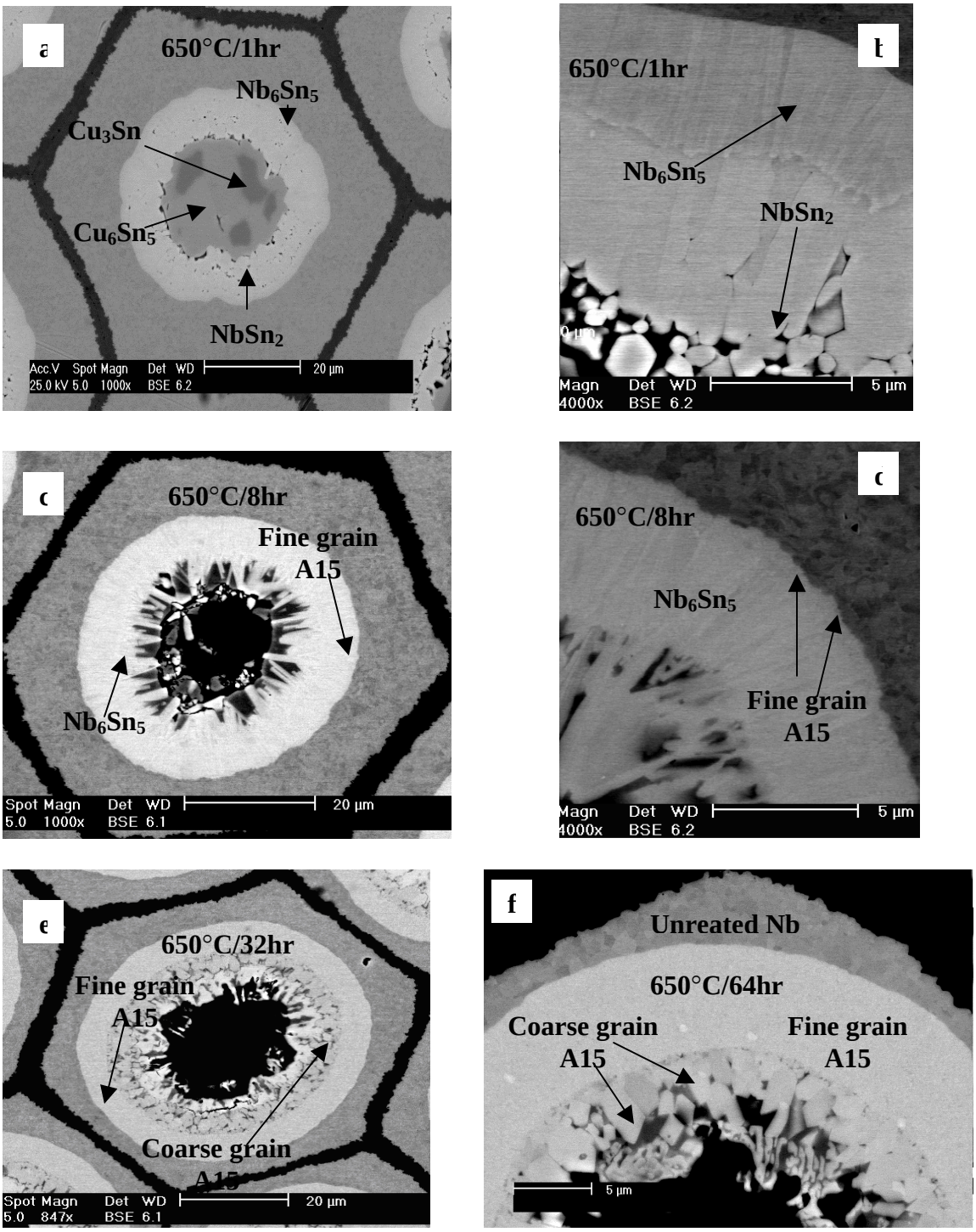

Figure 4.1(a-f) SEM-BSE micrographs of a subelement in sample S1 during microstructural phase evolution leading to A15 formation at 650°C after varying time intervals [43].

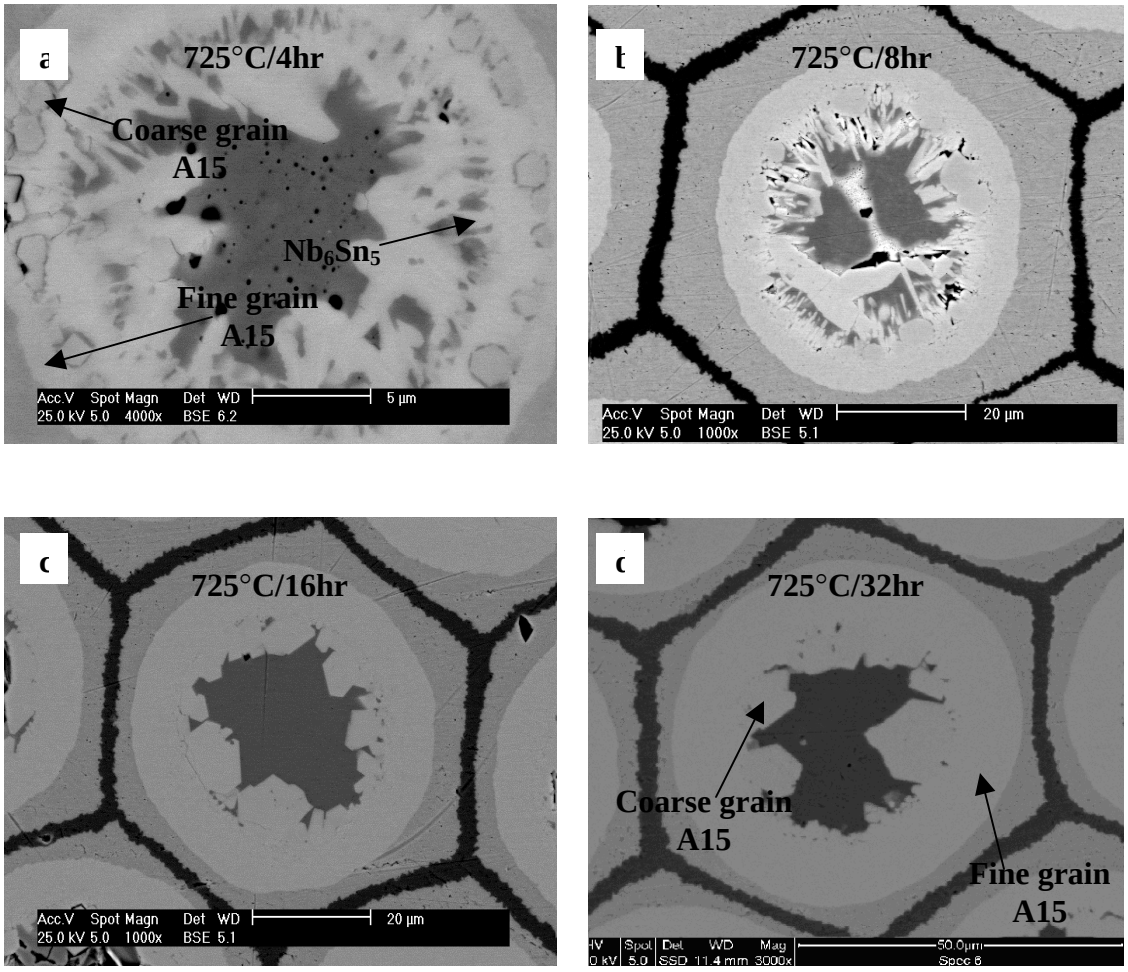

Figure 4.2(a-d) SEM-BSE micrographs of a subelement in sample S1 during microstructural phase evolution at 725°C after varying time intervals [43].

In strand S1, at longer reaction times (~250hours), the Sn tended to diffuse all the way through the Nb tube at some regions (typically the flats of the subelement due to its hexagonal shape). When the Sn atoms reached the Cu-Nb interface (between the subelement and the surrounding matrix), the Sn atoms would diffuse out from the A15 into the Cu matrix, and then re-enter the subelement along its outer periphery elsewhere,

forming a thin outer A15 shell by a reaction route similar to those in the internal-Sn or bronze conductors [38]. This was observed in Figure 4.3 in which sample S1 had been heat treated at 650°C for 250 hours. While this was essentially an unwanted parasitic effect that could be corrected by thicker Nb wall selection, it was interesting to note in Chapter 5 that this effect did lessen the stoichiometry of the A15 in sample S5 as a result of the loss of Sn in the surrounding Cu matrix. It also resulted in flux jumps and instabilities in the strand at higher magnetic fields due to an increase in the resistance of the Cu matrix caused by the Sn leak. This suggests that it may be useful to insert Sn-diffusion limiting layer such as a Ta barrier to maximize Nb_3Sn phase and prevent contamination of the surround matrix.

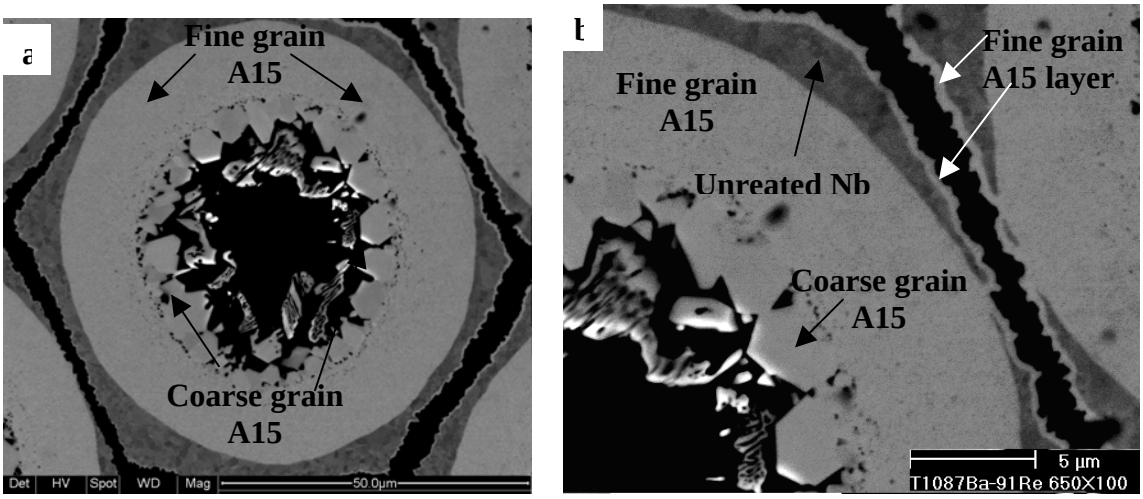

Figure 4.3 a) SEM-BSE Micrograph of a subelement of sample S1 heat treated at 650°C for 250 hours. b) A thin shell of A15 can be seen on the outer boundary due to Sn leak into the Cu matrix of the subelement while regions of the subelement were still unreacted.

4.3 A15 Layer Growth

The primary objective of investigating the Nb_3Sn growth kinetics was to facilitate a correlation between the amount of A15 formed and the heat treatment parameters. In the past a number of studies have addressed layer growth in internal-Sn and bronze conductors [59-64]. Some recent work had investigated layer growth in the A15 formed from Cu rich bronze alloys which tended to simulate growth in the bronze and internal-Sn composites [65-67]. It was observed that growth rates in these alloys were either controlled by the interface reaction or by the interdiffusion and were strongly dependent on the Sn composition as well as reaction temperature. However, while growth rates in PIT conductors have been well studied [29], growth rates in tube-type composites have not yet been studied in detail.

The layer thickness, l, of a compound formed during a diffusion process can be expressed as a power function of the reaction time t, according to equation (4.30) [68]. In the equation t_i is the incubation period or A15 start time, n is the growth exponent and k is the layer growth constant.

$$l = k\left(t - t_i\right)^n \tag{4.30}$$

It has been found theoretically that based on the values of the growth exponent n the rate controlling mechanism can be determined. When interface mobility is rate controlling n is unity and diffusion was found to occur simultaneously at higher rates [26]. If on the other hand bulk diffusion is rate controlling then n is 0.5 and layer growth follows the parabolic law. Any deviation from the above parabolic law for a diffusion

controlled process could be due to the influence of grain boundary diffusion, a changing microstructure, the finite system size, or cylindrical geometry of the subelement.

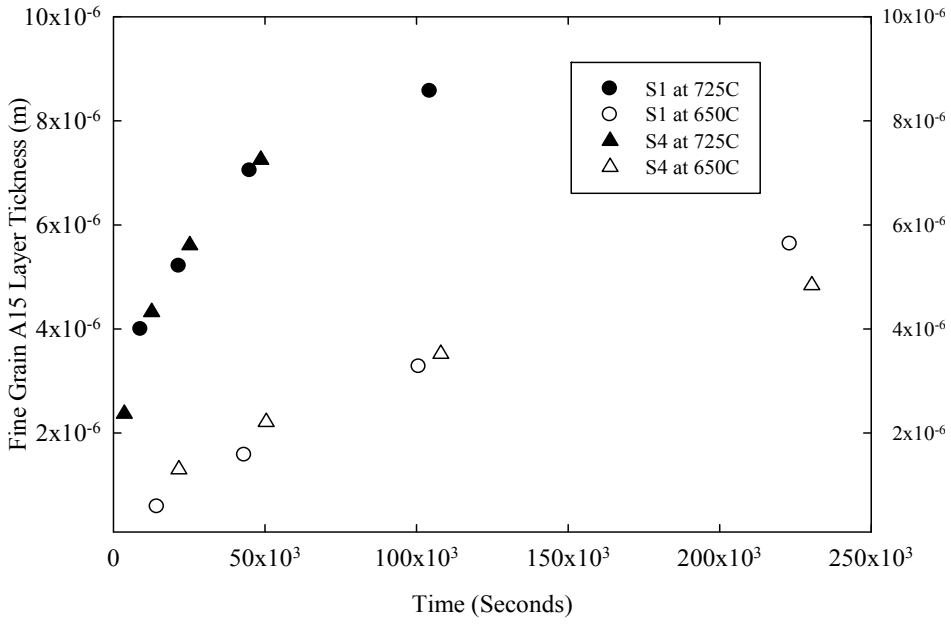

Figure 4.4 Plot of the layer thickness of the fine grain A15 as a function of reaction time measured across samples S1 and S4 heat treated at 650°C and 725°C.

Figure 4.4 shows a plot of the layer thickness of the fine grain A15 as a function of reaction time measured across samples S1 and S4 heat treated at 650°C and 725°C respectively. These values were the averages of measurements taken across three subelements. In an attempt to reduce the statistical uncertainties due to non uniform migration of the concentric boundary, area fractions were measured and then converted to an equivalent radii from which the thickness of the annulus were determined using Equation (4.31). Here $R_{A15/Nb}$ and $R_{Nb_6Sn_5/A15}$ were the radial distances from the centre of

the subelement up to the fine grain A15/Nb and Nb_6Sn_5/A15 boundaries respectively. In Figure 4.4 it was observed that the layer growth was a strong function of the reaction temperature and was relatively independent of the Sn content in the case of Sn rich Cu-Sn alloys. This was quite contrary to the A15 growth observed in bronze conductors which were sensitive to the initial Sn compositions [65-66]. At elevated temperatures, due to the increase in the kinetics, a significantly more rapid layer growth was observed.

The layer growth for the conductors of Ref [45] was apparently slower than that of internal-Sn, while our recent measurements on the present tube conductors shows a layer thickness of 4.5 μm at 650°C after 50 hours after A15 growth initiation (preceded by 4 h of 6:5 phase formation) [43], which compares to PIT values of 4.2 μm [45] under the same conditions (here the 6:5 formation time is not specified).

$$l = R_{A15/Nb} - R_{Nb_6Sn_5/A15} = \sqrt{\frac{A_{A15/Nb}}{\pi}} - \sqrt{\frac{A_{Nb_6Sn_5/A15}}{\pi}} \tag{4.31}$$

With the aid of a log-log plot in Figure 4.5 the layer growth exponent *n* and growth constant *k* were determined and are given in Table 4.1. Though the initial Sn composition did not affect layer growth rate appreciably, it did cause a change in the rate controlling process at 650°C. The exponent *n* in sample S1 at 650°C was found to be 0.72 indicating both Sn diffusion in the A15 and interface reactions were important. However, with higher Sn contents (sample S4) *n* decreased to 0.56 indicating a greater influence of interdiffusion on growth. An increase in the reaction temperature to 725°C was also observed to cause the growth exponent *n* to decrease. Hence, at higher temperatures

interdiffusion across the A15 layer was the rate controlling process for boundary migration with bulk diffusion dominating over grain boundary diffusion. This also suggested that interface reaction rates increased more rapidly than interdiffusion with temperature for sample S1.

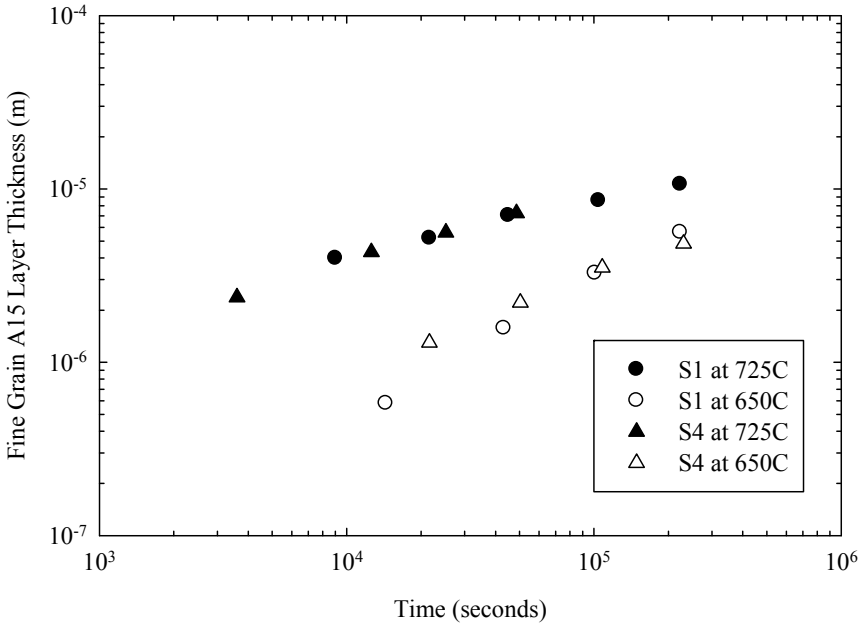

Figure 4.5 Log-Log plot of layer thickness as a function of reaction time for the fine grain A15 in sample S1 and S4 respectively.

Strand Name	Sn/Cu Area Ratio	650°C		725°C	
		n	*k*	*n*	*k*
S1	3.3	0.72	7.24×10^{-10}	0.53	2.52×10^{-8}
S4	6.3	0.56	4.93×10^{-9}	0.43	7.18×10^{-8}

Table 4.1 Contains the layer growth exponent *n* and growth constant *k* in samples S1 and S4 during heat treatment at 650°C and 725°C.

Differentiating equation (4.30), we can obtain, g, the growth rate

$$g = \frac{dl}{dt} = nk\left(t - t_i\right)^{n-1} \tag{4.33}$$

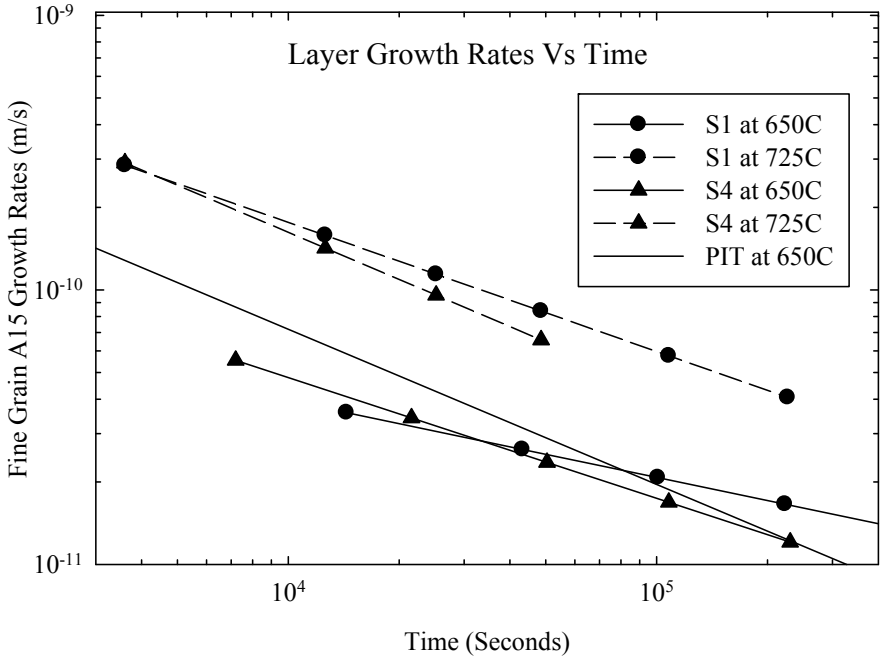

Figure 4.6 A plot of the fine grain A15 growth rate as a function of the reaction time at 650°C and 725°C measured across samples S1 and S4.

Figure 4.6 was a plot of the fine grain A15 growth rate which was calculated using equation (4.33) as a function of the reaction time at 650°C and 725°C on samples S1 and S4. A linear decrease in the growth rate was observed with reaction time. Growth rates were again independent of the initial composition but were strongly dependent on the reaction temperature, decreasing from $3.57\text{x}10^{-11}$ m/s to $1.37\text{x}10^{-11}$ m/s and $2.85\text{x}10^{-10}$ m/s to $4.84\text{x}10^{-11}$ m/s for sample S1 at 650°C and 725°C after 128 hours. Similar trends were also observed for sample S4 except that growth rates were slightly higher than those

of S1 at lower reaction times. The reaction rates obtained for PIT composites by S. Matafirri at the same reaction temperature were plotted for comparison in Figure 4.5 [45]. However, growth rates in the internal-Sn strands at 650°C were relatively low (~$5x10^{-12}$ m/s) [45]. These materials had lower Sn levels when compared to the recent HEP strands, which have higher growth rates [38].

4.4 Phase Formation Systematics and the Analytical Model

4.4.1 Introduction

In tube-type composites after complete reaction at temperatures between 650°C and 725°C the columnar Nb_6Sn_5 phase has been converted to coarse grain A15. The region just outside of this one is fine grain A15 that has formed in the surrounding Nb tube by Sn diffusion from the Nb_6Sn_5 layer. In order to optimize the performance of these composites it is necessary to maximize the fine grain A15 fraction and suppress the coarse grain fraction. In principle, this can be done by minimizing the growth of the Nb_6Sn_5 phase, since it is the phase that converts to coarse grain A15. Since the amount of Nb_6Sn_5 that forms increases with the amount of Sn present, lowering the Sn will lower the amount of Nb_6Sn_5 formed, however, if we reduce the amount of Sn too much, then the total amount of A15 is reduced. We will need, then, to estimate the optimal level of Sn needed, however this will vary with temperature. As discussed before the Nb_6Sn_5 growth ceases when the Sn content falls below ~27 at% as seen on the Cu-Nb-Sn ternary phase diagram [24]. This composition would vary with temperature, although how much variation in the regime of interest was not known. Moreover, for practical Nb_3Sn heat

treatments these values were well defined only at 675°C [26]. Hence investigation of the temperature dependence of phase formation as well as the initial subelement Sn/Cu ratio was of extreme importance as it controlled the supply and diffusion of Sn through the Nb tube and hence determined phase growth.

In this section, the extent of the coarse and fine grained A15 phase formed for samples with varying Sn/Cu area ratios were measured after complete reaction (Figure 4.7). The experimental results were compared with a simple analytical model [69] used to predict the A15 fractions for varying initial subelement Sn/Cu ratios. In order to optimize the heat treatment temperature, the amount of fine grain and coarse grain A15 formed for a given Sn/Cu ratio at different heat treatment temperatures after complete reaction was also analyzed.

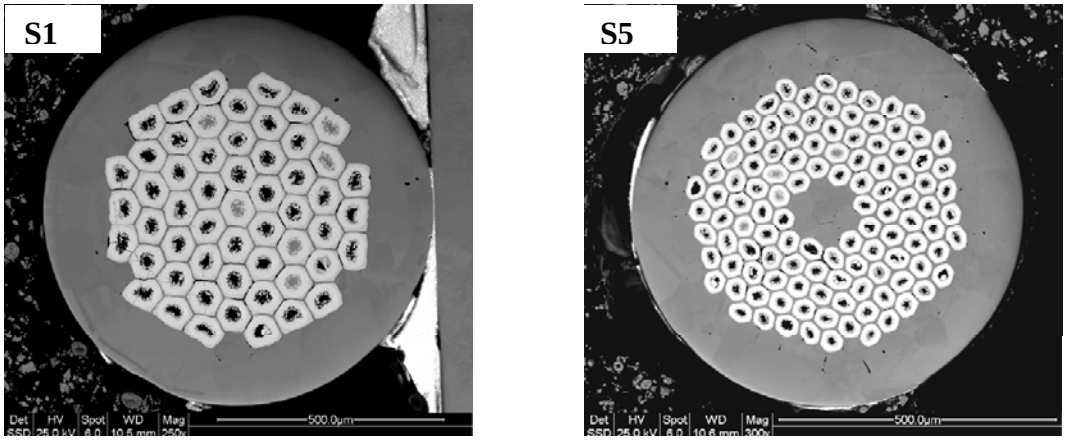

Figure 4.7 SEM-BSE micrographs of strand S1 and S5 after heat treatment at 675°C for 250 hours.

4.4.2 Comparison of the Analytical Model and Experimental Data

The first set of SEM analyses was performed on strands S1 to S5 (Table 3.1) heat treated at 675°C and the extent of phase formation was observed and quantified. Figures

4.8 and 4.9 shows the schematic sketch of the tube-type subelement at time t_o prior to reaction and after complete reaction (t_{A15}) respectively. Radii R_1 and R_2 are the boundaries of the unreacted Sn core and the Cu tube surrounding it. Radius R_5 is the outer boundary of the subelement. During the reaction the Nb rich region increases in size due to the addition of Sn to the region and the increase in the molar volume caused by the formation of the new phases, accordingly R_2 became R_{2f}. The boundary separating the coarse and fine grain regions of A15 is R_{3f}, this was also the boundary of maximum Nb_6Sn_5 growth. The maximum radius of fine grained A15 formed after complete reaction is R_4. The complete strand analysis for samples heat treated at 675°C for 250 hours was given in Table 4.2. The estimated error in measurement was ±0.7 μm.

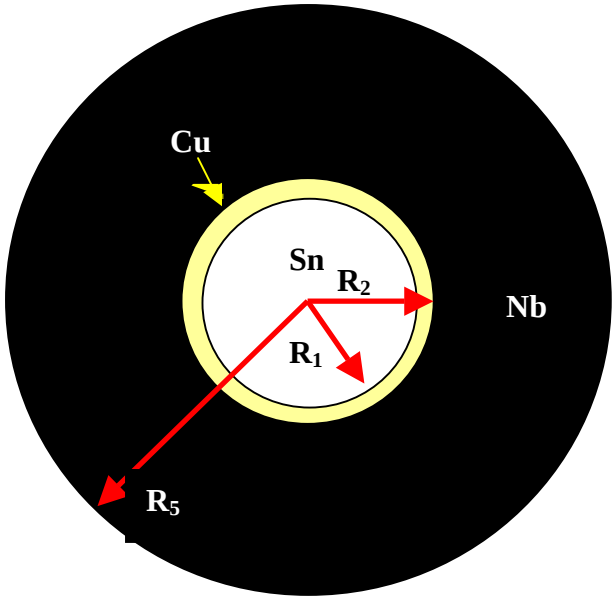

Figure 4.8 Schematic sketch of the tube-type subelement at time t_o prior to heat treatment.

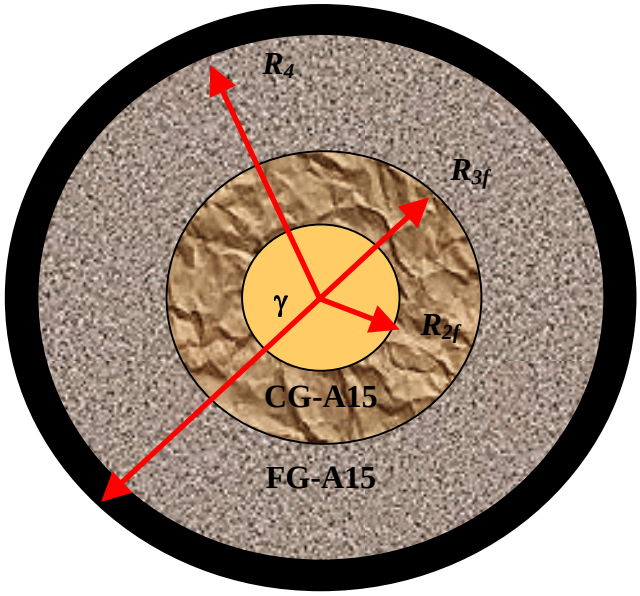

Time t_{A15} – Full reaction

Figure 4.9 Schematic sketch of the tube-type subelement after complete reaction (t_{A15}) showing the presence of coarse and fine grain A15 [69].

Strand Specification	S1	S2	S3	S4	S5
R_1 (R_{Sn}) : Sn radius at t_0 (μm)	14.2	12.8	10.9	8.6	9.6
R_2 (R_{Cu}): Cu radius at t_0 (μm)	16.2	14.3	11.8	9.2	10.2
R_{2f} : Nb-rich/Cu-Sn boundary at t_{A15} (μm)	12.3	9.8	8.1	6.5	7.6
R_{3f} : Coarse/Fine A15 t_{A15} (μm)	17.8	14.9	12.6	9.8	12.1
R_4 : A15 maximal extent (μm)	27.8	23.6	18.8	14.2	16.5
R_5 : Subelement radius (μm)	28.5	25.3	20.6	15.3	17.9

Table 4.2 Strand analyses conducted on samples S1 to S5 after complete reaction at 675°C for 250 hours

A simple analytical model was used to predict the location of the phase boundaries as well as the area fraction of the fine and coarse grain A15 phases formed after complete reaction [69]. With the aid of the model it was possible to determine radii R_{2f}, R_{3f} and R_4 which were correlated to the initially measured radii namely R_1 and R_2 given by equations (4.40-4.42).

$$R_{2F} = \sqrt{1.01R_2^2 - 0.728R_1^2} \tag{4.40}$$

$$R_{3F} = \sqrt{1.296R_1^2 + 0.0820R_2^2} \tag{4.41}$$

$$R_4 = \sqrt{1.99R_1^2 + R_2^2} \tag{4.42}$$

From these relations the area fraction could be determined using equations (4.43 - 4.45).

$$Area_{FG} = \pi\left(R_4^2 - R_{3F}^2\right) = 0.694R_1^2 + 0.918R_2^2 \tag{4.43}$$

$$Area_{CG} = \pi\left(R_{3F}^2 - R_{2F}^2\right) = 2.024R_1^2 - 0.928R_2^2 \tag{4.44}$$

$$Area_{TOT} = \pi\left(R_4^2 - R_{2F}^2\right) = 2.024R_1^2 - 0.928R_2^2 \tag{4.45}$$

The variation of the area fraction of the fine and coarse grain A15 (A_{CG}/A_{FG} and A_{FG}/A_{TOT}) with initial Cu-Sn compositions (R_{Sn}/R_{Cu}) was plotted in Figure 4.10 with the aid of the above set of equations and the experimental data in Table 4.2. This was fitted to the theoretical plot obtained from the analytical model. The experimental data seemed to be in good agreement with the theoretical fit.

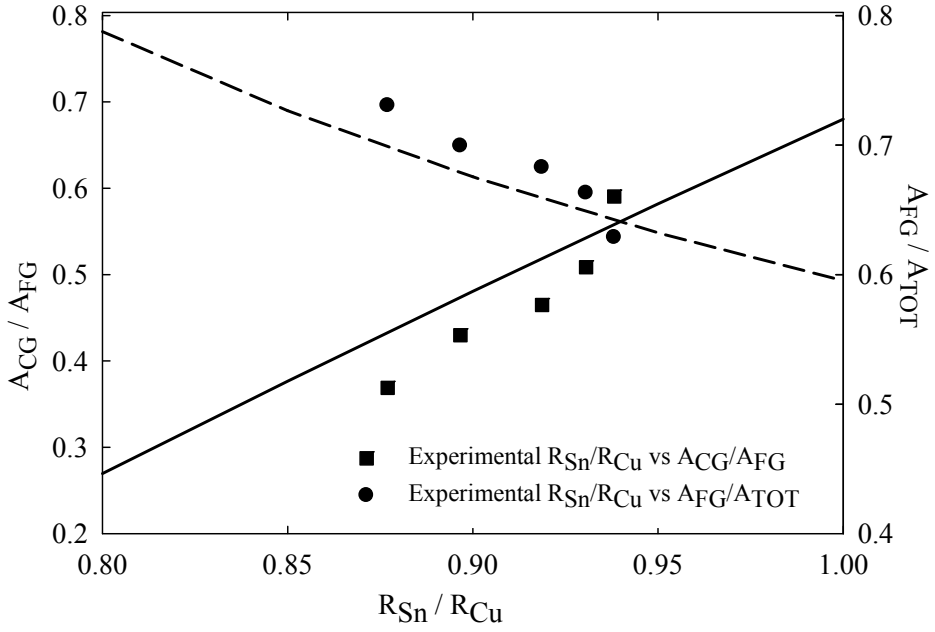

Figure 4.10 Variations of A_{CG}/A_{FG} (solid line theory, squares experimental data) and A_{FG}/A_{TOT} (dotted line theory, circles experimental data) with R_{Cu}/R_{Sn} measured across samples S1 to S5 after heat treatment at 675°C.

An increase in the initial R_{Sn}/R_{Cu} ratio resulted in an increase in the A_{CG}/A_{FG} ratio and a subsequent decrease of the A_{FG}/A_{TOT} ratio. This was primarily due to greater supply of Sn from the central core to the Nb tube resulting in a larger radial growth of Nb_6Sn_5 which then converted to coarse grain A15. Hence at higher Sn contents the growth of fine grained A15 was suppressed. However the initial Sn level must be optimized as a significant reduction in the Sn content will cause a reduction in the total A15 area fraction and an increase in the area fraction of the unreacted niobium tube.

4.4.3 Effect of Temperature on the Coarse/Fine A15 phase fractions

Figure 4.11 shows the variation of the fine and coarse grain A15 area fraction with temperature for sample S1 having a fixed Sn/Cu ratio. It was observed that as the reaction temperature increased the A_{CG}/A_{FG} ratio increased linearly where as the A_{FG}/A_{TOT} ratio decreases linearly. Hence the use of a higher heat treatment temperature caused enhanced radial growth of Nb_6Sn_5 which resulted in an increase in the area fraction of the coarse grain A15. This implied a shift in the ternary phase diagram from the values at 675°C such that lower Sn, Cu-Sn phases were in coexistence with Nb_6Sn_5 at these higher temperatures. Hence at temperatures higher than 675°C the switch from Nb_6Sn_5 to A15 formation began at composition lower than 27 at% Sn.

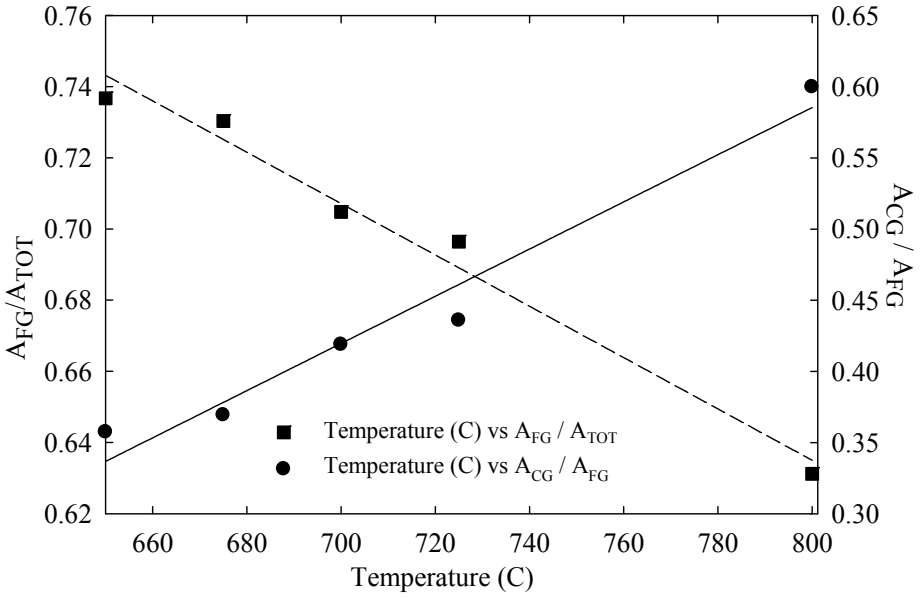

Figure 4.11 Variation of A_{CG}/A_{FG} (circles experimental data, fitted with solid line) and A_{FG}/A_{TOT} (squares experimental data, fitted with dotted line) with temperature for strand S1.

CHAPTER 5

COMPOSITIONAL AND MICROSTRUCTURAL ANALYSIS OF THE A15

5.1 Introduction

The Nb_3Sn phase exists over a composition range from about ~18 to ~25 at% Sn with superior properties being found at the stoichiometric composition. In our case the formation of the A15 phase is by the process of reactive diffusion of the Sn atoms through the coaxial Nb tube with Cu aiding in the A15 formation in the temperature range of 650-725°C. The real reason is that the Nb_6Sn_5 is rich in Sn and thus so is the subsequently formed coarse grain A15. But the fine grain is formed by reactive diffusion, and since the A15 is not a line compound, this is bound to lead to lower Sn contents. Of course, such compositional gradients were bound to affect the superconducting properties such as the critical temperature T_c as well as the critical magnetic field B_{c2} [8]. These gradients could be reduced by heat treating the system to equilibrium using long time, elevated temperature heat treatments. Such heat treatments would result in an increase in the grain sizes of both the fine and coarse grain A15 grains with reaction time thereby causing a reduction in the critical current density J_c. Thus there exists a fine balance

between obtaining an optimum stoichiometry in the A15 and the fine grain size (100-200nm) needed for strong flux pinning.

To facilitate further conductor development and enhance the performance boundaries of these composites it is necessary to characterize them in terms of their microstructure and microchemistry. In this section compositional analysis was performed on tube-type stands to correlate the effect of heat treatment temperature on the Sn gradient across the fine and coarse grain A15. The effect of the initial subelement Sn/Cu ratio on the Sn gradients was also studied for a given heat treatment temperature. A detailed study of the of the grain morphology and grain growth of both the fine and coarse grain A15 was also investigated with the aid of fracture SEM samples. The activation energy for grain growth was also calculated from the experimental data.

5.2 Effect of Heat Treatment Temperature on the A15 Composition

As discussed earlier the critical parameters of the Nb_3Sn superconductors can be strongly correlated to the Sn concentrations across the A15 phase. The main advantage of the tube type composites is the larger fraction of the Sn rich A15 phase compared to the bronze route, and the smaller filaments possible as compared to the internal-Sn route. The subelement sizes present in these conductors permitted detailed analyses of the Sn gradients across the A15 phase by the SEM-EDS technique.

Compositional analysis was carried out by the SEM-EDS details of which were discussed in Chapter 3. This analysis was performed on sample S1 heat treated at temperatures between 650°C and 800°C for 250 hours and is given in Table 3.3. Figure

5.1 shows the spots at which measurements were taken across the coarse and fine grain A15. Interaction volume calculated from the Monte Carlo simulation indicated a spherical region of diameter 0.85 to 1.6 microns at 15 kV [58].

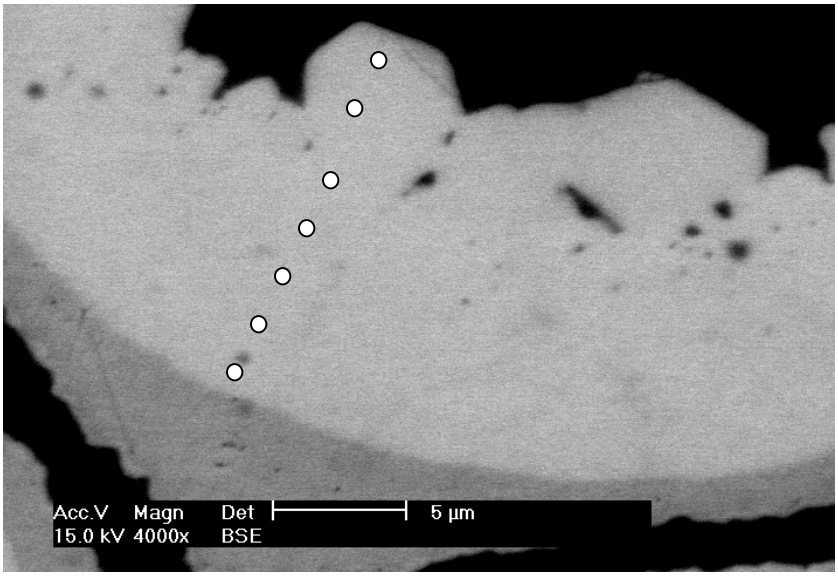

Figure 5.1 Electron beam spot positions taken across the A15 layer in subelement of S1, reacted at 650°C for 250 hours. Distances were measured with respect of the coarse/fine interface.

Prior to measurement the detector was calibrated with the aid of a bulk sample of known composition [57] the "standard sample". Also EDS measurements on the unreacted Nb tube indicated the presence of about 4-5 at% Ta which was uniformly distributed. Figure 5.2 shows the typical EDS energy spectra obtained at an accelerating voltage of 15 kV after about 60 seconds of collection time. Figure 5.2a corresponds to the measurements across the standard sample containing peaks of Nb and Sn. The error in measurement was approximately 0.12%. Figure 5.2b, an EDS spectrum measured on sample S1 in the fine grain region on at a location of 3 µm from the interface after heat

treatment at 650°C for 250 hours, showed the presence of Nb, Sn, Ta and Cu atoms. However the exact location of the Cu atoms could not be identified.

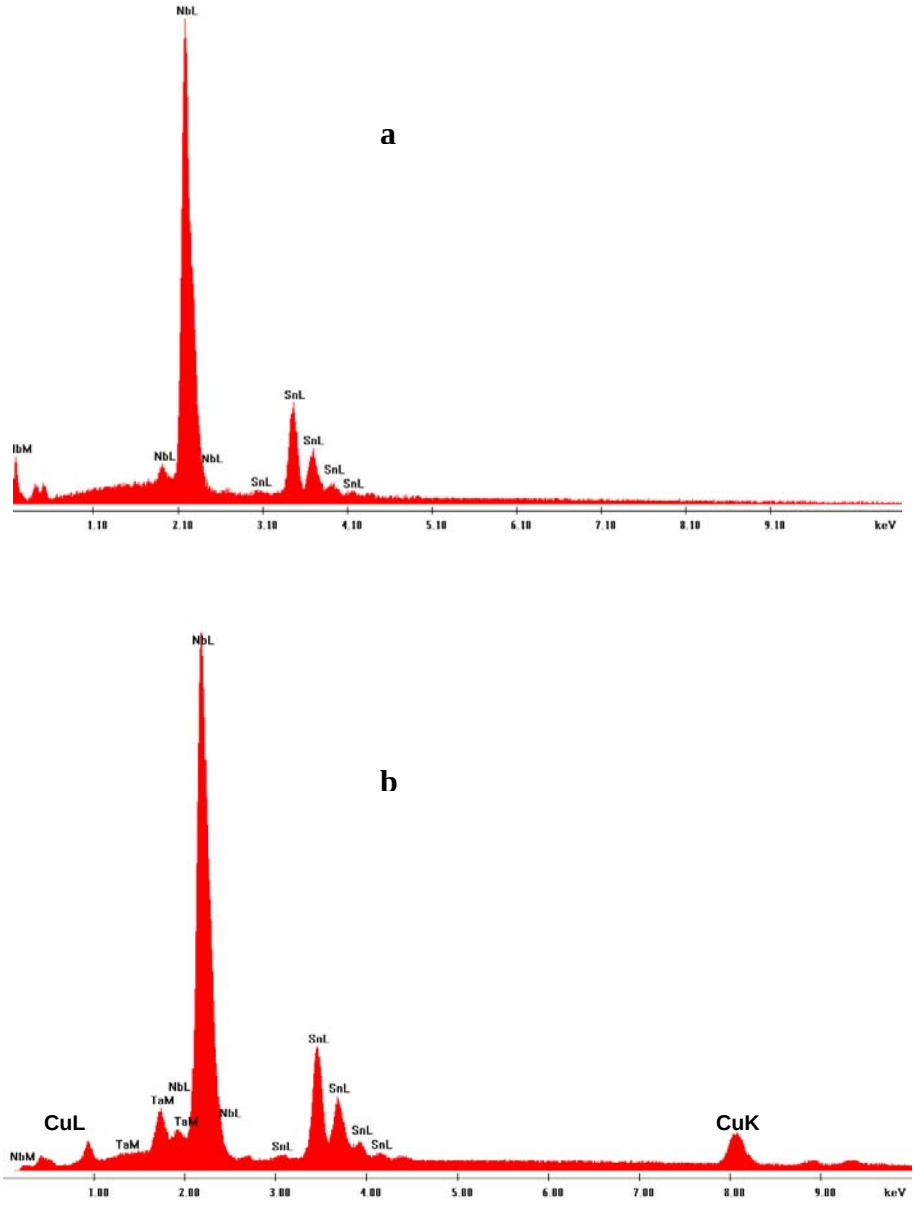

Figure 5.2 SEM-EDS spectrum a) Measured across the standard sample indicating about 24.88 at% Sn and 75.12 at% Nb b) Measure on sample S1 after heat treatment at 650°C in the fine grain region

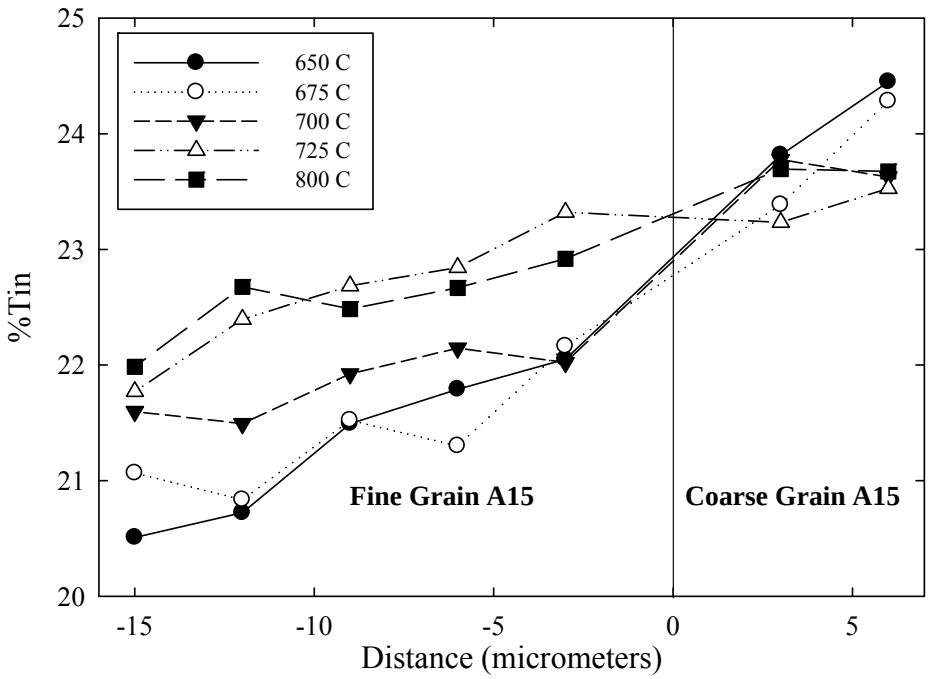

Figure 5.3 Variation of Sn compositions with radial distance for strand S1 at various temperatures. The vertical line represents the boundary between the coarse and fine grain regions. Distances were measured from the coarse/fine interface.

The average variation of Sn with average radial distance with respect to the coarse/fine grain A15 interface is as shown in Figure 5.3. These measurements were conducted on sample S1 heat treated for 250 hours at various temperatures. Sn gradients were found to vary from approximately 0.2 at% Sn/μm at 650°C to about 0.085 at% Sn/μm at 800°C across the A15 layer. Such measurements were also performed by C.D.Hawes on ternary PIT strand which showed gradients of about 0.3 at% Sn/μm [29]. There was also a small increasing Sn gradient observed across the fine grain A15 as we moved inwards, while steeper gradients were observed across the coarse and fine grain

interface at lower temperatures. The Sn content in the coarse grain A15 was found to be greater than the fine grain A15 at all reaction temperatures. At higher temperatures the difference between the Sn levels in the fine and coarse grain A15 seemed to decrease as a result of homogenization caused by an increase in the diffusion kinetics. In particular at higher reaction temperatures the Sn content in the fine grain A15 had increased, while that in the coarse grain had decreased. This could be due to faster diffusion of the Sn atoms from the coarse grain to the fine grain areas at these elevated temperatures.

5.3 Effect of the Initial Sn/Cu ratio on the A15 Composition

Composition profiles were obtained across the filaments similar to that shown in Figure 5.1 using SEM-EDS. Figure 5.4 shows the variation of the Sn content across samples S1, S3 and S5 with various initial Sn/Cu ratios and varying subelement diameters after complete reaction (250 hours) at 725°C. As discussed in the previous section similar Sn gradients were observed across all three filaments. An increase in the initial Sn/Cu ratio did cause a slight increase in the Sn content in the coarse grain A15; however the Sn content across the fine grain A15 remained relatively unaffected. This was also consistent with the B_{c2} data (Table 5.1) which showed no increase with increasing initial subelement Sn compositions. The significantly lower Sn values observed for sample S5 having a filament diameter of about 35 μm were attributed to Sn loss to the Cu matrix at prolonged reaction times. This was also confirmed with the aid of EDS spectra in Figure 5.5 indicating about 2-3 at% Sn in the Cu matrix. This also highlighted the importance of filament diameter and strand design while optimizing the heat treatment.

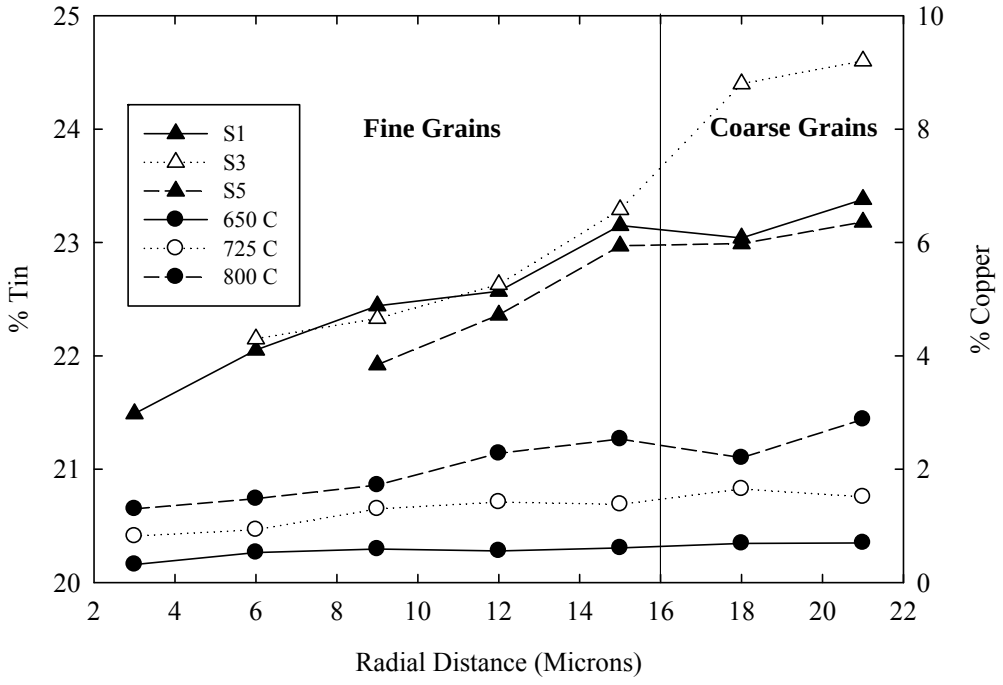

Figure 5.4 Variation of the % Sn across the subelements of sample S1, S3 and S5 heat treated at 675°C for 250 hours. Distances were measured with respect to the outer boundary of the fine grain A15. Additionally, variation in at% Cu in the A15 is shown across sample S1 at various temperatures.

5.4 Analysis of the Cu levels in the A15 with Temperature

As seen in Figure 5.4 the Cu content across the A15 layer measured across sample S1 was observed to be strongly dependent on the reaction temperature. The Cu content increased from about 0.5 at % to about 2.5 at % with a temperature change from 650 to 800°C. However, it could not be determined whether the Cu was present in elemental form, as second phase particles or in solution with the A15 as this would require TEM/STEM analysis.

M. Suenaga through his previous investigation on bronze conductors using Auger electron microscopy showed that Cu was relatively insoluble in the A15 and was present at the grain boundary in its elemental form at room temperature [34-35, 70]. He found up to 15 at% Cu at the grain boundaries in bronze conductors. A similar situation presumably exists in these studies.

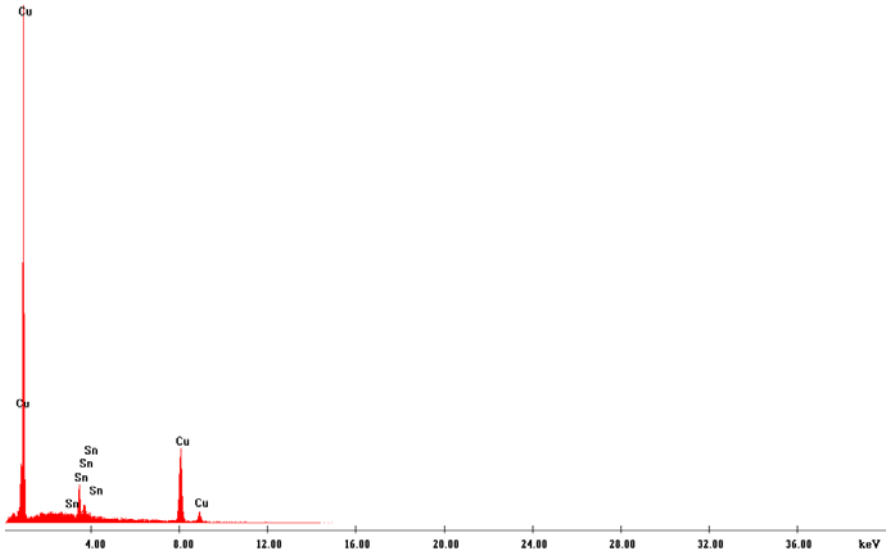

Figure 5.5 EDS spectra in the Cu matrix at a distance of 4 microns from the subelement interface, indicating about 2-3 at% Sn leak.

5.5 Grain Growth and Morphology of the A15

In order to achieve high critical current densities by strong flux pinning it becomes necessary to maximize the fraction of the fine grain A15 and minimize the grain size. Grain boundaries, precipitates, solute atoms and dislocation cell walls all act as pinning centers. For such microstructural features to act as pinning centers it is required that its spatial extent be greater than the coherence length at least in one dimension [71].

Grain size analysis was performed on fracture samples with the aid of the FESEM operating in the ultra high resolution (UHR) mode. Figure 5.6 shows the fractographs of strand S1 after reaction at 650°C and 800°C after 250 hours. Substantial grain growth was observed in both the coarse and fine grained A15 at elevated temperatures. At 650°C after complete reaction some amounts of what appeared to be Cu-Sn intermetallics were also observed in the central region of the filaments however these intermetallics were not observed at elevated temperatures.

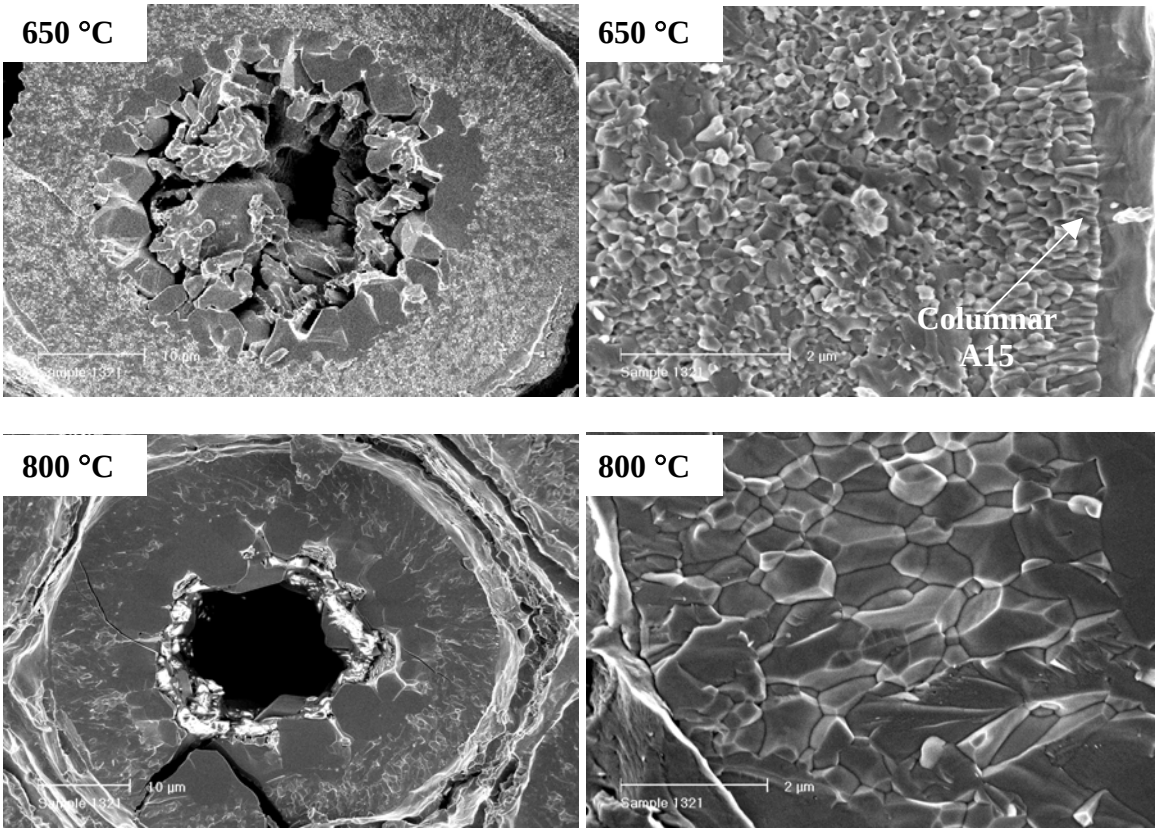

Figure 5.6 Fracture SEM obtained with an FESEM operating in the UHR mode on sample S1 at 650°C and 800°C indicating significant grain growth of the fine grain A15 at 800°C.

The fine grained A15 was observed to be relatively equiaxed at 650°C however at elevated temperatures there was a considerable change in the aspect ratio of these grains which tended to be columnar in shape. Even at 650°C, the equiaxed fine grains were surrounded by columnar A15 (Figure 5.7 a) at the outer boundary where the Sn content had decreased to about 21 at% as observed from the EDS measurements. Such columnar grains due to depletion of Sn were also observed by several authors in composites manufactured by the bronze process and PIT techniques [21]. Hence the depletion of Sn as well as elevated temperature heat treatments causes a significant increase in the aspect ratio of the A15 grains. This increase in aspect ratio and preferential growth of these grains in the diffusion direction strongly suggests a decrease in the A15 nucleation rate. Large amount of grain growth in the direction of diffusion was observed in the fine grain A15 at 800°C. Moreover the coarse grain A15 layer was found to be a single grain thick (Figure 5.7b).

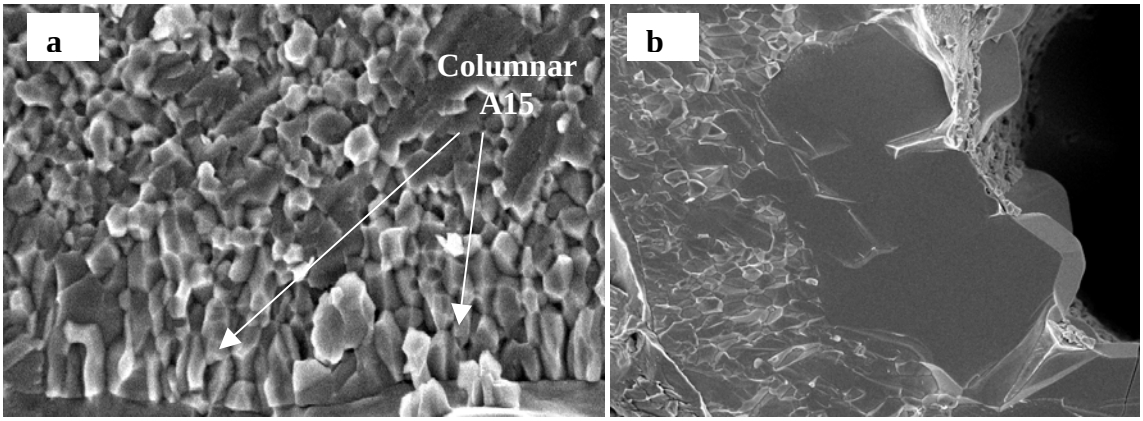

Figure 5.7 Fracture SEM micrographs a) Shows the presence of columnar A15 grains on the outer boundary where the Sn levels were about 21 at% at 650°C b) Shows the grain growth in the coarse grain A15 at 800°C which was a single grain thick.

Figure 5.8 shows the variation of grain size with reaction temperature for the fine and coarse grain A15 in sample S1. Grain size was quantified in terms of its diameter, *d*, which was calculated by first measuring the areas of about 20 grains, taking the average, and then extracting *d* approximating the grains as round. The error bars in Figure 5.8 were determined from the standard deviations of these data sets. Both the coarse grain as well as the fine grain A15 sizes increased rapidly with increasing reaction temperature. The fine grain size increased from 150 nm to about 800 nm while the coarse grain A15 increased from 300 μm to about 900 μm with increase in reaction temperature from 650 to 800°C. Figure 5.9 shows the variation in grain size with reaction temperature for samples with varying initial Sn/Cu of 3.3 and 7.5 (samples S1 and S5) after 250 hours. No significant differences in grain size were observed for subelements with different initial Sn/Cu ratios.

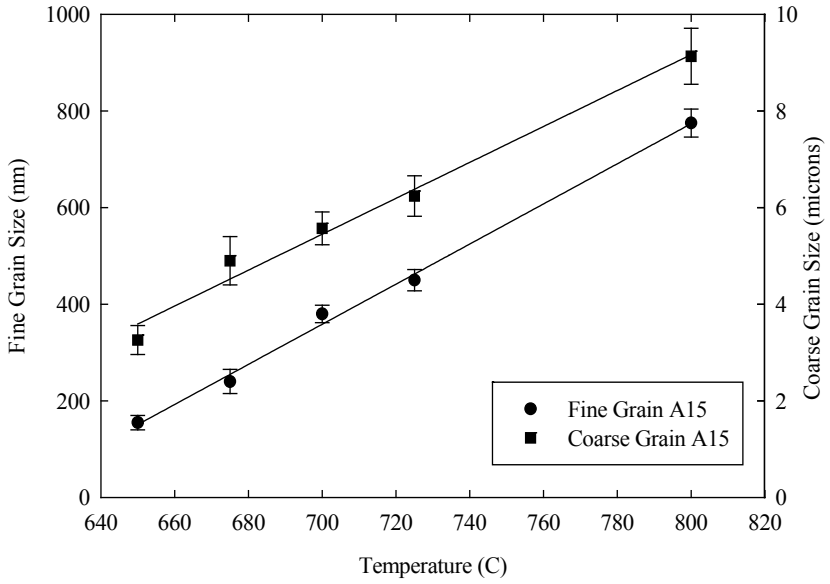

Figure 5.8 shows the variation of grain size with temperature for the fine and coarse grain A15 across S1, errors bars were also marked to indicating the deviation in measurement.

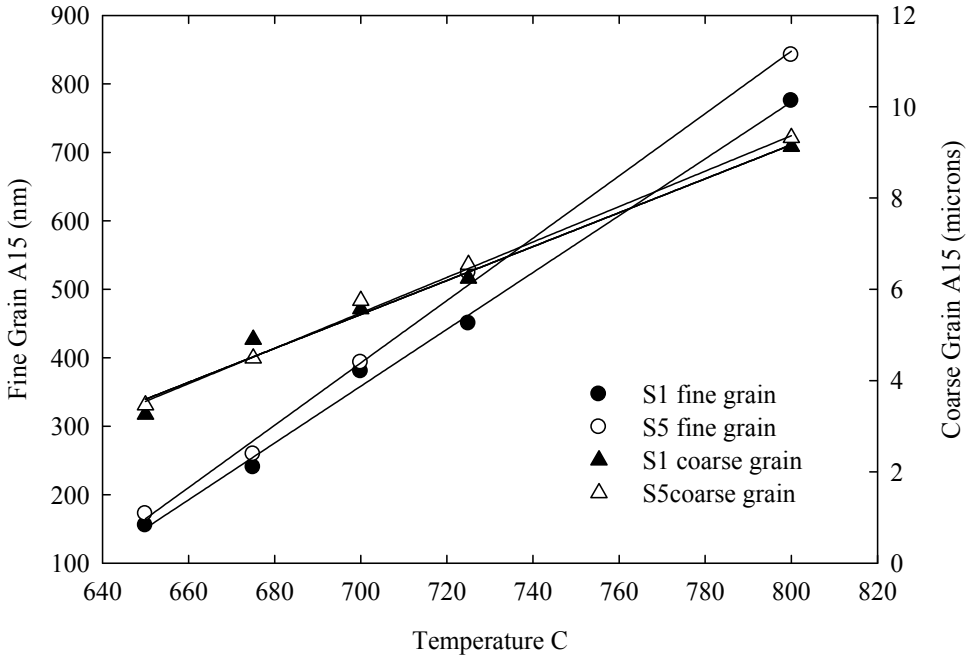

Figure 5.9 shows the variation in grain size with reaction temperature for samples with varying initial subelement Sn/Cu ratios measured across S1 and S5 after 250 hours.

5.6 Activation Energy for Grain Growth

Figure 5.10 shows the activation energy for grain growth of the coarse and fine grain A15. This was calculated based on the grain growth equations (5.60-5.62) where d is the diameter after time t, d_0 is the initial diameter at time $t = 0$, k is the grain growth constant and Q was the activation energy [72]. Assuming curvature driven growth and that the initial grain size prior to grain growth was negligibly small compared to the final grain size after grain growth the activation energy was obtained from a plot of Ln (d^2/t) versus ($1/T$) in Figure 5.10.

$$d^2 - d_0^2 = kt \tag{5.60}$$

$$k = k_0 \exp(\frac{-Q}{RT}) \tag{5.61}$$

$$\frac{d^2}{t} = k_0 \exp(\frac{-Q}{RT}) \tag{5.62}$$

The activation energy for the growth of the coarse grain A15 was about 101.4 kJ/mole. At lower temperatures up to about 675°C the activation energy for growth of the fine grain A15 was 267.7 kJ/mole, however at a certain intermediate temperature between 675-700°C (cannot be accurately predicted due to the lack of data points) there appeared to be a kink leading to a significantly decreased value of 125 kJ/mole.

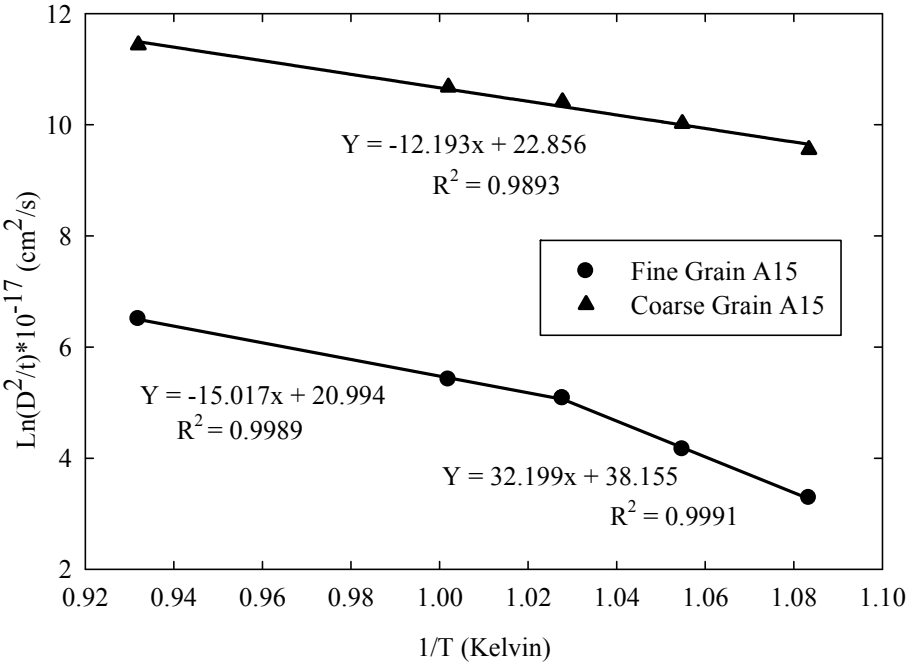

Figure 5.10 Plot of activation energy for grain growth of the fine and coarse grain A15. A kink was observed for the activation energy in the fine grain A15 at a temperature in between 675-700°C.

5.7 Strand Properties- J_c and B_{c2}

Critical current density J_c is defined as the critical current I_c that flows in the non-Cu section of the wire per unit cross sectional area. The non-Cu J_c values for strands S1 to S5 heat treated at 675°C for an optimum time interval given in Table 3.3 are as shown in Figure 5.11. Non-Cu J_c was found to vary from about 1800 A/mm^2 to about 2300 A/mm^2 at 12 T. For transport measurements, the heat treatment was chosen to react as much of the Nb tube as possible without reacting fully through it. These measurements were carried out by the ITER barrel technique discussed in Chapter 3.

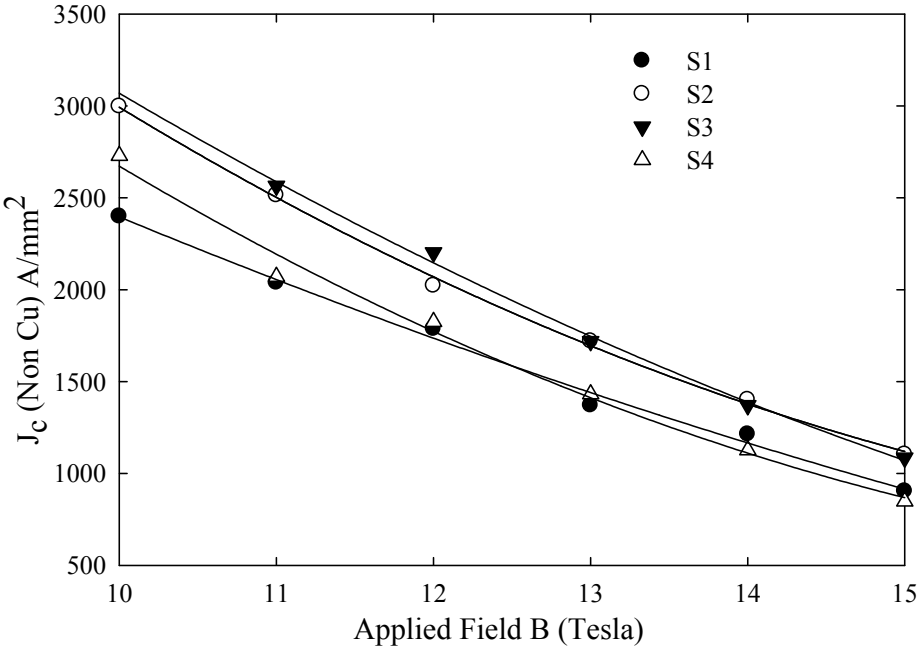

Figure 5.11 Non-Cu J_c values for the strands S1 to S5 heat treated at 675°C for an optimum time interval.

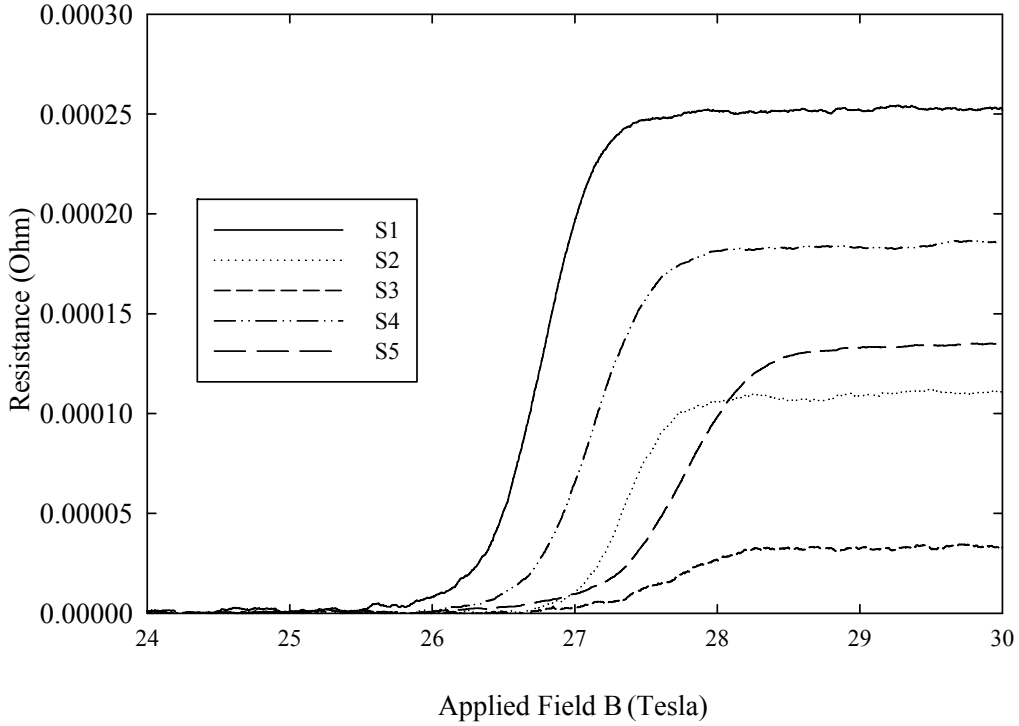

Figure 5.12 Plot of the variation of the sample resistance with applied magnetic field for strands S1 to S5 heat treated at 675°C for 250 hours.

Figure 5.12 shows the variation of the samples resistance with applied magnetic field for samples S1 to S5 heat treated at 675°C for 250 hours. Theses measurements were performed at National High Magnetic Field Laboratory (NHMFL) at Tallahassee, Florida. Table 5.1 gives the B_{c2} values for all the five strands heat treated at 675°C and 725°C. In all cases a slight increase in B_{c2} was observed with increasing temperature which was mainly due to the increase in Sn content in the fine grain A15 as well as a more homogenous Sn profile (Figure 5.3). The decrease in B_{c2} due to the increased Cu

content across the A15 layer at elevated temperatures (Figure5.4) was not observed. Moreover there was clear correlation of the B_{c2} data with the initial subelement Sn/Cu ratio.

Strand name	T1 = 675 °C		T2 = 725 °C	
	0.1 of Transition	0.9 of Transition	0.1 of Transition	0.9 of Transition
S1	26.3	27.1	26.5	27.1
S2	26.3	26.9	27.0	27.7
S3	25.9	26.5	27.1	28.1
S4	26.3	27.1	26.7	27.1
S5	25.7	26.5	27.2	28.2

Table 5.1 Resistance transition data obtained for stands S1 to S5 heat treated at 675°C and 725°C for 250 hours. An increase in B_{c2} was observed with temperature for all five strands.

CHAPTER 6

CONCLUSION

Tube-type Nb_3Sn composites fabricated using Nb-7.5wt% Ta alloy tubes with varying subelement Sn/Cu ratios have been studied in terms of their phase formation and reaction systematics. These conductors were found to have non-Cu critical current densities (J_c) ranging from 1800-2300 A/mm^2 at 12 T and upper critical fields (B_{c2}) of about 26-28 T. During heat treatment, the liquid Cu-Sn alloy reacted with the coaxial Nb tube forming the A15 compound via the $NbSn_2$ and Nb_6Sn_5 intermetallic phases, with some similarities to PIT conductors. At elevated reaction temperatures of about 725°C and for higher initial subelement Sn/Cu ratios, the incubation time for the fine grain A15 formation was observed to be lower.

Unlike the bronze and internal-Sn composites the layer growth in tube-type composites was insensitive to the initial subelement Cu-Sn alloy composition. They were also (like Bronze and internal Sn) strongly dependent on the reaction temperature. Interdiffusion was primarily the rate controlling mechanism for the layer growth of the fine grain A15, however, in sample S1 at 650°C the effects of interface reaction on layer growth were observed. Interfacial effects were also observed in the growth of the coarse grain A15 at the Nb_6Sn_5/fine grain A15 interface resulting in localized growth.

The experimental data on phase formation was compared to a simple analytical model and shown to be in good agreement with a deviation of less than ±5%. Additionally, it was shown that lower temperatures lead to larger fractions of the conductor being fine grain A15. Also the use of higher Sn/Cu ratios enhanced the growth of the coarse grain A15.

Compositional analysis of the Sn profiles across sample S1 indicated a strong dependence on the reaction temperature between 650-800°C. Sn gradients across the A15 layer were found to vary from approximately 0.2 at% Sn/μm at 650°C to about 0.085 at% Sn/μm at 800°C. Thus more homogenous profiles and greater Sn contents in the fine grain A15 were observed at elevated temperatures. Also greater levels of Cu were detected in the A15 matrix at higher reaction temperatures. The grain size of the fine grain A15 increased linearly with temperature; however there was also an increase in the aspect ratio of these grains. No significant changes in the morphology or grain size were observed with change in composition of the initial subelement Cu-Sn alloy. At an intermediate temperature between 675°C and 700°C there appeared to be a reduction in the activation energy for grain growth of the fine grain A15. The typical decrease in B_{c2} with lower reaction temperatures was also observed.

LIST OF REFERENCES

[1] T. Pyon and E. Gregory, *IEEE Trans. on Appl. Supercond*., vol. **11**, pp.3688-91 (2001).

[2] J. A. Parrell, Y. Zhang, M. B. Field, P. Cisek and S. Hong, *IEEE Trans. on Appl. Supercond*., vol. **13**, pp.3470-3 (2003).

[3] A. den Ouden, S. Wessel, E. Krooshoop and H. ten Kate*, IEEE Trans. Appl. Supercond.*, vol. **7**, pp.733-738 (1997).

[4] P. J. Lee, C. M. Fischer, M. T. Naus, M. C. Jewell, A. A. Squitieri, and D. C. Larbalestier, *IEEE Trans. Appl. Supercond.*, vol. **13**, pp.3422-3425 (2003).

[5] B. T. Matthias, T. H. Geballe, S. Geller and E. Corenzwit, *Phys. Rev.,* vol. 95, pp.1435-8 (1945).

[6] J.W. Ekin, *J. Appl. Phys*., vol. **62,** pp.4829 (1987).

[7] R. M. Scanlan, *IEEE Trans. Appl. Supercond.*, vol. **11**, pp.2150-2155 (2001).

[8] H. Devantay, J. L. Jorda, M. Nindel, B. Obst and R. Flukinger, *J. Mat. Sci.*, vol. **16**, pp.2145-2153 (1981).

[9] K. Tachikawa, T. Asano, and T. Takeuchi, *Appl. Phys. Lett.,* vol. **39**, pp.766-68 (1981).

[10] J. D. Livingston *IEEE Trans. on Magnetics,* vol. **14**, pp.611 (1978).

[11] M. Suenaga, C. J. Klamut, N. Higuchi and T. Kuroda, *IEEE Trans. on Magnetics,* vol. **21**, pp.305-308 (1985).

[12] K. Tachikawa, H. Sekine and Y. Iijima, *J. of Appl. Phys.,* vol. **53**, pp.5354 (1982).

[13] M. Suenaga, K. Tsuchiya and N. Higuchi, *Appl. Phys. Lett.,* vol. **44**, pp.919 (1984).

[14] H. K. Onnes, *Leiden Communication,* vol. **120** (1911).

[15] K. Fossheim and A. Sudhbo, *Superconductivity Physics and Applications*, John Wiley and Sons Ltd. (2005).

[16] V. L. Ginzburg and E. A. Andryshin, *Superconductivity*, World Scientific Publishing Co. Pte. Ltd. (2005).

[17] W. Meissner and R. Ochsenfeld, "Ein neuer Effekt bei Eintritt der Supraleitfähigkeit," *Naturwissenschaften,* vol. **21**, p. 787 (1933).

[18] A.C Rose-Innes and E. H. Rhoderick, *Introduction to Superconductivity*, 2nd ed. Pergamon, Oxford (1978).

[19] J. Bardeen, L. N. Cooper, and J. R. Schrieffer, "*Theory of Superconductivity*," *Phys. Rev.,* vol. **108**, pp.1175 (1957).

[20] R. W. Cahn and P. Haasen, *Physical Metallurgy*, 4th ed. vol. **2**, (1996).

[21] A. Godeke, "*Performance Boundaries in Nb_3Sn Superconductors*" PhD. Thesis, University of Twente, (2005).

[22] R. Mailfert, B.W. Batterman, and J. J. Hanak, *Phys. Lett*., vol. **24A**, pp.315-16 (1967).

[23] V. Guritanu, W. Goldacker, F. Bouquet, Y. Wang, R. Lortz, G. Goll and A. Junod, *Phys. Rev B*, vol. **70B**, pp.184526 (2004).

[24] J. P. Charlesworth, I. MacPhail, and P. E. Madsen, *J. of Mat. Sci.,* vol. **5**, p.580 (1970).

[25] H. J. Okamoto, *J. Phase Equilib.*, vol. **24**, pp.390 (2003).

[26] W. L. Neijmeijer, "*Microstructural and Kinetic Studies of the Manufacturing of Superconducting Nb_3Sn*" PhD thesis, University of Twente, Netherlands, (1988).

[27] J. H. L. Lindenhovius and E. M. Hornsveld, *IEEE Trans. on Appl. Supercond*., vol. **10**, pp.975-978 (2000).

[28] C. Fischer, "*Investigation of the Relationships between Superconducting Properties and Nb_3Sn Reaction Conditions in Powder in Tube Nb_3Sn Conductors*" PhD thesis, The University of Wisconsin-Madison (2002).

[29] C. Hawes, "*Investigations of a Inhomogeneity of a Powder in Tube Nb_3Sn Superconductor*" PhD thesis, The University of Wisconsin-Madison, (2000).

[30] K. Tachikawa, Y. Kuroda, H. Tomori and M. Ueda, *IEEE Trans. Appl. Supercond*., vol. **7,** pp.1355-9 (1997).

[31] C. D. Hawes, P. J. Lee and D. C. Larbalestier, *Supercond. Sci. Technol*., vol. **19**, pp.27-37 (2006).

[32] X. Wu, X. Peng, M. D. Sumption, M. Tomsic, E. Gregory and E. W. Collings, *Adv. Cryog. Eng*. vol. **824,** pp.504-12 (2006).

[33] S. Foner and B.B. Schwartz, *Superconductor Material Science*, Plenum Press, New York (1980).

[34] M. Suenaga, and W. Jansen, *Appl. Phys. Lett*. vol. **43,** pp.791-3 (1983).

[35] D. Smathers and D. C. Larbalestier, *Adv. Cryo. Engg. Mat*., vol. **28**, pp.415-419 (1982).

[36] M. C. Jewell, A. Godeke, P. J. Lee and D.C. Larbalestier, *Adv. Cryog. Engg*., vol. **50B**, pp474-8 (2004).

[37] R. Flukiger, *Atomic Ordering, Phase Stability and Superconductivity in Bulk and Filamentary A15 Type Compounds*, (1987).

[38] R. Dhaka, "*Sn and Ti Diffusion, Phase Formation, Stoichiometry and Superconducting Properties of Internal-Sn Type Nb_3Sn Conductors*" MS thesis, The Ohio State University, (2007).

[39] A. R. Kaufmann and J. J. Pickett, *Bulletin American Phys. Society,* vol. **15**, pp.838 (1970).

[40] L. D. Cooley, C. M. Fisher, P. J. Lee and D. C. Larbalestier, *J. of Appl. Phys.,* vol. **96**, pp.2122-30 (2004).

[41] J. D. Elen, C.A.M van Beijnen, C.A.M van der Klein, *IEEE Trans. on Magnetics*, vol. **13**, pp.470-3 (1971).

[42] T. Wong and C. V. Renaud, *IEEE Trans. on Appl. Supercond*., vol. **11**, pp.3584-7 (2001).

[43] V. R. Nazareth, M. D. Sumption, X. Peng, E. Gregory, M. J. Tomsic, and E. W. Collings, *IEEE Trans. on Magnetics*, (Accepted for publication).

[44] V.R. Nazareth, M. D. Sumption, X. Peng, E. Gregory, M. J. Tomsic and E.W. Collings, *ICMC Conference 2007* (Accepted for publication).

[45] E. Barzi, and S. Mattafarri, *IEEE Trans. on Appl. Supercond*., vol. **13**, pp.3414-7 (2003).

[46] S. Murase, M. Koizumi, O. Horigami, H. Shiraki, Y. Koike, E. Suzuki, M. Ichihara, M. Nakane and N. Aoki, *IEEE Trans. on Magnetics*, vol. **15**, pp.83-86 (1979).

[47] D. Rodrigues Jr. and J. P. B. Machado, *Materials Research*, vol. **3**, pp.99-103 (2000).

[48] H. Yamasaki, M. Umeda, M. Watanabe and Y. Kimura, *J. Appl. Phys*., vol. **53**, pp.7479-85 (1982).

[49] C. Renaud, L. R. Motowidlo and T. Wong, *Adv. Crog. Eng.,* vol. **50**, pp.376-381 (2004).

[50] M. Nagata, Okuda, and M. Kawashima et al., *Adv. Cryog. Eng.,* vol. **28**, pp.791-796 (1982).

[51] H. Yamasaki and Y. Kimura, *Cryogenics,* vol. **22**, pp.89-94 (1982).

[52] S. Murase, Y. Koike and H. Shiraki, *J. of Appl. Phys.,* vol. **49**, pp.6020-26 (1978).

[53] E. Gregory, *ICMC Conference 2007.*

[54] J. W. Ekin, *Experimental Techniques for Low Temperature Measurements*, Oxford University Press (2007).

[55] P. J. Goodhew and F. J. Humphreys, *Electron Microscopy and Analysis*, 2nd ed., Taylor and Francis Inc. (1988).

[56] B. D. Cullity "*Elements of X-Ray Diffraction*", 2nd ed., Addison-Wesley Co., (1978).

[57] W. Goldacker, R. Ahrens, M. Nindel, B. Obst, C. Meingast, *IEEE Trans. Appl. Supercond.,* vol. **3**, pp.1322-1325 (1993).

[58] P. Hovington, D. Drouin, and R. Gauvin, *Scanning 19*, vol. **1**, pp.1-14 (1997).

[59] H. Veringa, P. Hoogendam, and A. C. A. Wees, *IEEE Trans. Appl. Magn*., vol. **19**, pp.773-6 (1983).

[60] M. T. Naus, P. J. Lee and D. C. Larbalestier, *IEEE Trans. Appl. Supercond.,* vol. **11**, pp.3569-72 (2001).

[61] P. J. Lee, A. A. Squitieri and D. C. Larbalestier, *IEEE Trans. Appl. Supercond*. vol. **10**, pp.979-82 (2000).

[62] C. A. M. Beijnen and J. D. Elen, *IEEE Trans. on Magn.*, vol. **15**, pp.87-90 (1979).

[63] M. Suenaga, O. Horigami and T. S. Luhman, *Appl. Phys. Lett.*, vol. **25**, pp.624-7 (1974).

[64] V. Diadiuk, J. Bostock and M. L. A. Macvicar, *IEEE Trans. on Magnetics,* vol. **1**, pp.610-2 (1979).

[65] Y. Muranishi, M. Kajihara, *Mater. Sci. Eng. A*, vol. **404**, pp.31-41 (2005).

[66] Y. Tanaka, M. Kajihara, Y. Watanabe, *Mater. Sci. Eng. A*, vol. **445-446**, pp.355-63 (2007).

[67] T. Hayase and M. Kajihara, *Mater. Sci., Eng. A*, vol. **433**, pp.83-89 (2006).

[68] J. H. Westerbook and R. L. Fleischer, *Intermetallic compounds-principles and practice,* vol. **1**, John Willey and Sons Ltd., (1995)

[69] M. D. Sumption, *unpublished*.

[70] D. Rodrigues Jr., C. L. H. Thieme, D. G. Pinatti, and S. Foner, *IEEE Trans. Appl. Supercond*., vol. **5**, pp.1607-10 (1995).

[71] F. Buta, "*Phase Evolution and Superconducting Properties of Nb-Al Superconductors processed by a Rapid Heating/Quenching Method*" PhD thesis, The Ohio State University, (2003).

[72] R. E. Reed-Hill, *Physical Metallurgy Principles*, PWS-Kent publishers 3rd ed., pp. 202-207 (1992).